Biomechanics and Modeling in Mechanobiology (2025) 24:1223–1250
https://doi.org/10.1007/s10237-025-01963-6

ORIGINAL PAPER

Image-based computational hemodynamics in the right heart

Francesca Renzi[1,3] · Giovanni Puppini[2] · Giovanni B. Luciani[1] · Christian Vergara[3]

Received: 12 September 2024 / Accepted: 10 April 2025 / Published online: 11 June 2025

Abstract
Characterizing flow within the right heart (RH) is particularly challenging due to its complex geometries. However, gaining insight into RH fluid dynamics is of extreme diagnostic importance, given the high prevalence of acquired and congenital heart diseases with impaired RH function. In this proof-of-concept study, we propose a pipeline for patient-specific simulations of RH hemodynamics. We reconstruct the geometry and motion of the patient's right atrium, ventricle, and pulmonary and tricuspid valves, from multi-series cine MRI. For this purpose, we develop a novel and flexible reconstruction procedure that, for the first time, integrates patient-specific tricuspid valve dynamics into a computational model, enhancing the accuracy of our RH blood flow simulations. We apply this approach to study the hemodynamics in both healthy and repaired-ToF RH with severe pulmonary regurgitation, as well as to assess the hemodynamic changes induced by the pulmonary valve replacement intervention. Modeling the entire RH enables us to understand the contribution of the superior and inferior vena cava inflows to the ventricular filling, as well as the impact of the impaired right atrial function on the ventricular diastole. To analyze the turbulent and transitional behavior, we include the large eddy simulation sigma model in our computational framework, which reveals how the contribution of the smallest scales in the dissipation of the turbulent energy changes among health and disease.

Keywords Right heart · Tetralogy of Fallot · Pulmonary regurgitation · Computational fluid dynamics · Patient-specific analysis · In silico simulations

1 Introduction

The right heart (RH) significantly impacts many congenital and acquired heart disorders (Dumitrescu et al. 2018). Among all, the Tetralogy of Fallot (ToF) is the most common cyanotic congenital heart disease, occurring in approximately 1 in 3,500 births and accounting for about 10% of all congenital malformations (Buechel and Mertens 2012). Infants affected by such pathology undergo a reparative surgery in their first months of birth to restore the correct blood oxygenation (repaired-ToF). Although the survival rate after the intervention has improved markedly over the years (Cuypers et al. 2014), repaired-ToF patients often exhibit surgical sequelae such as chronic pulmonary insufficiency, residual right ventricular outflow tract obstruction (RVOTO), or scarring (Pass and Cohen 2023). These problems can lead to several other complications in adulthood, including severe pulmonary regurgitation (PR), right ventricle (RV) dilation or hypertrophy, biventricular dysfunction, and arrhythmias (Redington 2006), to name a few. These dramatically hamper life quality, leading to RH dysfunction

✉ Francesca Renzi
francesca.renzi@univr.it

Giovanni Puppini
giovanni.puppini@aovr.veneto.it

Giovanni B. Luciani
giovanni.luciani@univr.it

Christian Vergara
christian.vergara@polimi.it

[1] Department of Surgery, Dentistry, Paediatrics and Gynaecology, University of Verona, Piazzale Ludovico Scuro 10, 37134 Verona, VR, Italy

[2] Department of Diagnostic and Public Health, University of Verona, Piazzale Ludovico Scuro 10, 37134 Verona, VR, Italy

[3] LaBS, Dipartimento di Chimica, Materiali e Ingegneria Chimica "Giulio Natta", Politecnico di Milano, Piazza Leonardo da Vinci 12, 20133 Milano, MI, Italy

and eventually heart failure, which calls for the need for additional surgical interventions in adulthood, e.g., through pulmonary valve replacement (PVR). In particular, among all the late outcomes, PR and residual RVOTO stand out as the most important, as it has been shown to be linked to RV remodeling processes (Redington 2006; Senthilnathan et al. 2013; Freling et al. 2014). For these reasons, the appropriately timed PVR intervention is of utmost importance in halting the RV remodeling and allowing RH function recovery. Nowadays, the main tools for assessing RV remodeling, as well as PR and RVOTO, are cardiac magnetic resonance imaging and echocardiography. However, both technologies do not provide a comprehensive analysis of intracardiac flow pre- and post-PVR (Senthilnathan et al. 2013). In contrast, computational fluid dynamics (CFD) models, when suitably adjusted to the available patient's data, could allow for the detailed measurement of hemodynamics alteration following such intervention, offering a valuable understanding of the surgical outcomes in both the short and long term.

Developing in silico models for the RH of repaired-ToF patients is a particularly challenging task due to the need to account for both the variability of the cardiac morphology and the specific cardiac wall movement. The first requirement is met by building patient-specific computational models, which provide insight into local cardiac hemodynamics and have proved informative in addressing various queries in other clinical contexts as well (Biglino et al. 2017; Fumagalli et al. 2024). To address the second requirement, the literature presents two approaches that differ in how they recover the cardiac chamber's displacement. In the case of fluid–structure interaction (FSI) models, the displacement is an unknown of the problem (Bucelli et al. 2023; Viola et al. 2022). These models are generally characterized by high computational costs, require meticulous calibration of the myocardial properties, and need to recover the unloaded configuration. In the second approach, the displacement can be prescribed either from offline electromechanical simulations (Augustin et al. 2016; Zingaro et al. 2024) or from images. In the latter case, we talk about dynamic image-based CFD (DIB-CFD) models (Bennati et al. 2023b; Chnafa et al. 2016; Fumagalli et al. 2022; Seo et al. 2014; Wiputra et al. 2016; Mangual et al. 2012; Collia et al. 2021). Despite the main drawback of complex image processing needed to recover a meaningful and artifact-free cardiac movement, this approach has become a valid alternative to the FSI model when detailed dynamical images are available. Regarding the study of ToF, both FSI (Tang et al. 2010) and DIB-CFD models (Wiputra et al. 2018; Loke et al. 2022, 2024) have been recently developed for the study, e.g., of turbulence and stresses characterizing such condition.

So far, DIB-CFD works on RH have solely focused on either the ventricular (Mangual et al. 2012; Wiputra et al. 2018; Loke et al. 2022, 2024) or the atrial chamber (Mareels et al. 2004; de Oliveira et al. 2021; Parker et al. 2022), separately. However, we observe that the presence of the right atrium (RA) ensures the correct inflow to the RV in diastole without requiring assumptions about the flow and the velocity profile at the tricuspid valve orifice. On the other side, accurately describing the diastolic phase is crucial to initialize systole in terms of blood velocity and pressure fields. Thus, we claim that including both chambers is fundamental for the accurate and comprehensive analysis of the whole cardiac cycle.

Knowing that RH efficiency depends on the RA–RV interplay, modeling both chambers is also especially crucial in the context of ToF, where it has been proved that the RA performance is an independent predictor for adverse outcomes post-PVR (Ali et al. 2019; Ait-ALi et al. 2020). Previous DIB-CFD studies also neglected the presence of (and thus the interaction with) the pulmonary and tricuspid valves (PV and TV). This omission could represent a significant limitation, as blood dynamics is highly influenced by the interaction with valves, especially in pathological cases and in the context of PVR. In the direction of overcoming these limitations, a first step was performed in Renzi et al. (2025), where we presented a novel technique for RH reconstruction from multi-oriented cine MRI. This technique was then tested in a complete RH, where, however, only the systolic phase was considered, and the valve dynamics was approximated by an on/off behavior.

In the present study, we want to overcome the previous limitations by developing a comprehensive DIB-CFD model based on time-resolved cine MRI of the whole right heart (RV + RA + TV + PV). Specifically, we simulate the whole heartbeat, including the patient-specific dynamics of the valves and their interaction with blood. Thanks to these new elements, we provide a deep analysis of the hemodynamic changes that occur immediately after the implantation of a competent PV in severely regurgitant repaired-ToF patients. For this purpose, we study the hemodynamics in three different scenarios, namely a healthy and two repaired-ToF cases. We compare some of our results with reference literature values and, for the regurgitant repaired-ToF case, with available phase-contrast MRI (PC-MRI) measurements at the pulmonary valve outflow tract.

In this respect, the main contributions of this work are:

1. The development of fully RH patient-specific DIB-CFD simulation for the whole heartbeat with imposed motion of ventricle, atrium, pulmonary artery root, pulmonary and tricuspid valves, all reconstructed from cine MRI;
2. The in silico investigation of hemodynamics changes right after PVR;
3. The analysis of blood stagnation-related quantities (e.g., blood residence time) which were never investigated in the context of RH;

4. The introduction of new insights into the comparison between the right and left hemodynamics.

The new aspects of this research enable us to bring forth an original computational analysis for the repaired-ToF and to underscore the suitability of the reconstruction method proposed in Renzi et al. (2025) for DIB-CFD modeling.

2 Methods

In this section, we detail the image processing procedure for the reconstruction of the patient-specific RH geometries and tricuspid and pulmonary valves, and we present the mathematical model for the description of the blood flow within the whole RH and its interaction with the endocardial walls and the valves. Finally, we introduce the quantities of interest obtained by post-processing the numerical results.

2.1 Available clinical data

Clinically indicated and ad hoc cardiac cine MRI studies were performed for two subjects at the Division of Radiology, University Hospital Verona, Verona, Italy. In particular, we have at disposal images for:

- a healthy subject, hereafter referred to as H;
- a patient with chronic pulmonary valve insufficiency (regurgitant fraction, RF, computed from the volumes obtained processing the cine MRI series, equal to 38%) after the repair of tetralogy of Fallot in infancy, with dilated RV and mild TV stenosis (hereafter referred to as ToF).

Ethical review board approval and informed consent were obtained from both subjects. The acquisitions were performed using Achieva 1.5T (TX)—DS (Philips, Amsterdam, the Netherlands) technology—and consist of slices with homogeneous in-plane spatial resolution ranging from 1.15 to 1.25 mm and thickness ranging from 5 to 8 mm. All series have a time resolution of 30 frames/cardiac cycle. In particular, the dataset is composed of the following cine MRI series: short-axis (SA), four-chamber long-axis (4Ch-LA), three-chamber LA (3Ch-LA), and two-chamber LA (2Ch-LA). In addition, for H, we have rotational images over the tricuspid valve (TV-R), at our disposal. This dataset enables the complete reconstruction of the right atrium (RA), right ventricle (RV), right ventricle outflow tract (RVOT), main pulmonary artery (PA), as well as the tricuspid (TV) and pulmonary (PV) valves. We refer the reader to Renzi et al. (2025) for a detailed description of the used dataset.

Additionally, for ToF we also have a 2D phase-contrast MRI (PC-MRI) acquisition on a plane at the level of the pulmonary valve outflow tract. The 2D PC-MRI is characterized by a temporal resolution of 20 frames in one cardiac cycle, an in-plane pixel resolution of 1.25×1.25mm, a slice thickness of $8mm$, and a velocity encoding value of 200 cm/s. In the present work, these data are used as clinical evidence for comparing the simulated and the patient's flows.

2.2 Reconstruction of right heart geometry and motion

In this study, we obtain the geometries of RH internal walls and their motion over the cardiac cycle employing the MSMorph procedure presented in Renzi et al. (2025) and specifically developed for the generation of patient-specific RH configurations from differently oriented cine MRI acquisitions. Figure 1 shows a schematic representation of the whole pipeline. Briefly, we segment the right atrial and ventricular endocardia on each slice of all cine MRI series at disposal for every acquired time instant. The segmentation is performed in a semiautomatic fashion by applying a non-rigid B-Spline-based image registration algorithm implemented in the open-source library `SimpleElastix` (https://simpleelastix.github.io/). Then, we collect the segmented contours referring to the same time instant to obtain N sets of atrial and ventricular endocardium contours, being N the total number of frames of the cine MRI acquisitions (see Fig. 1—step 1). In the second step, we deform a template surface over each set of contours to recover two separate representations of the atrial and ventricular endocardial surfaces (Fig. 1—step 2). Then, we compute the RA and RV deformation fields obtained with respect to the reference end-systolic configuration by employing another non-rigid B-Spline-based registration algorithm in `SimpleElastix` (Fig. 1—step 3).

Finally, we built the surface mesh at the reference end-systolic configuration, starting from the connection of RA and RV surfaces. This allows us to obtain the meshes at each frame n by applying the deformation fields previously computed and suitably extended to the TV annulus (see Fig. 1 bottom panel).

All these geometric preprocessing steps were obtained with the software Vascular Modeling Toolkit (`vmtk`, http://www.vmtk.org/, Antiga et al. 2008), enriched by additional tools for the cardiac surface processing (Fedele and Quarteroni 2021).

2.3 Reconstruction of tricuspid valve geometry and motion

In this section, we present a new procedure for the generation of patient-specific TV geometry and motion, as outlined in Fig. 2. The main novelty of our procedure is that it does

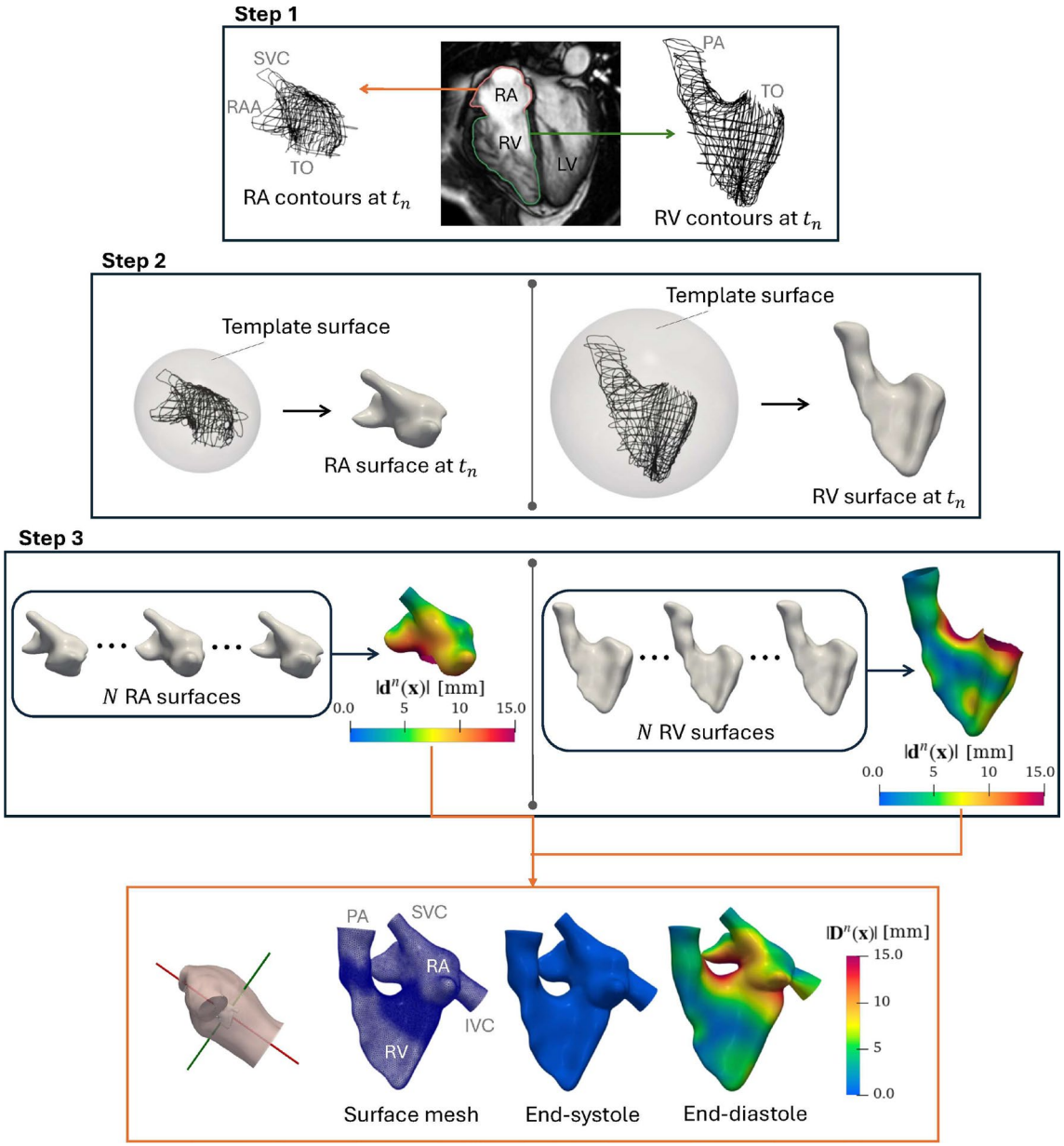

Fig. 1 Flowchart of the reconstruction procedure for the RH (Sect. 2.2). Step 1: representation of the endocardial segmentation at frame t_n; step 2: representation, at frame t_n, of the RA and RV endocardial surface generated starting from a template and the segmented contours; step 3: representation of the generation of the RA and RV displacement, $\mathbf{d}^n(\mathbf{x})$, with respect to a reference configuration, starting from the N surfaces (output of step 2); the magnitude of the computed displacement at the end-diastolic frame is showed; orange box: final results of the procedure: RH surface mesh obtained for the reference end-systolic configuration (left), application of the displacement field, $\mathbf{D}^n$, computed for the end-systolic (center) and end-diastolic (right) frame. IVC: inferior vena cava; LV: left ventricle; PA: pulmonary artery; RA: right atrium; RAA: right atrial appendage; RV: right ventricle; SVC: superior vena cava; TO: tricuspid orifice

not rely on rotational acquisitions—consisting of 18 views, evenly rotated around the axis that connects the center of the atrioventricular valve orifice to the ventricular apex—such as rotational cine MRI (Stevanella et al. 2011; Bennati et al. 2023b) or transthoracic real-time three-dimensional echocardiography (Votta et al. 2008). Instead, it integrates information from any available cine MRI series in which the valve is visible by exploiting the deformation of a template.

In particular, to recover the patient-specific TV leaflets' morphology and motion over the heartbeat, the proposed procedure comprises the following steps which are depicted in Fig. 2:

1. The segmentation of the TV leaflets on the available cine MRI;

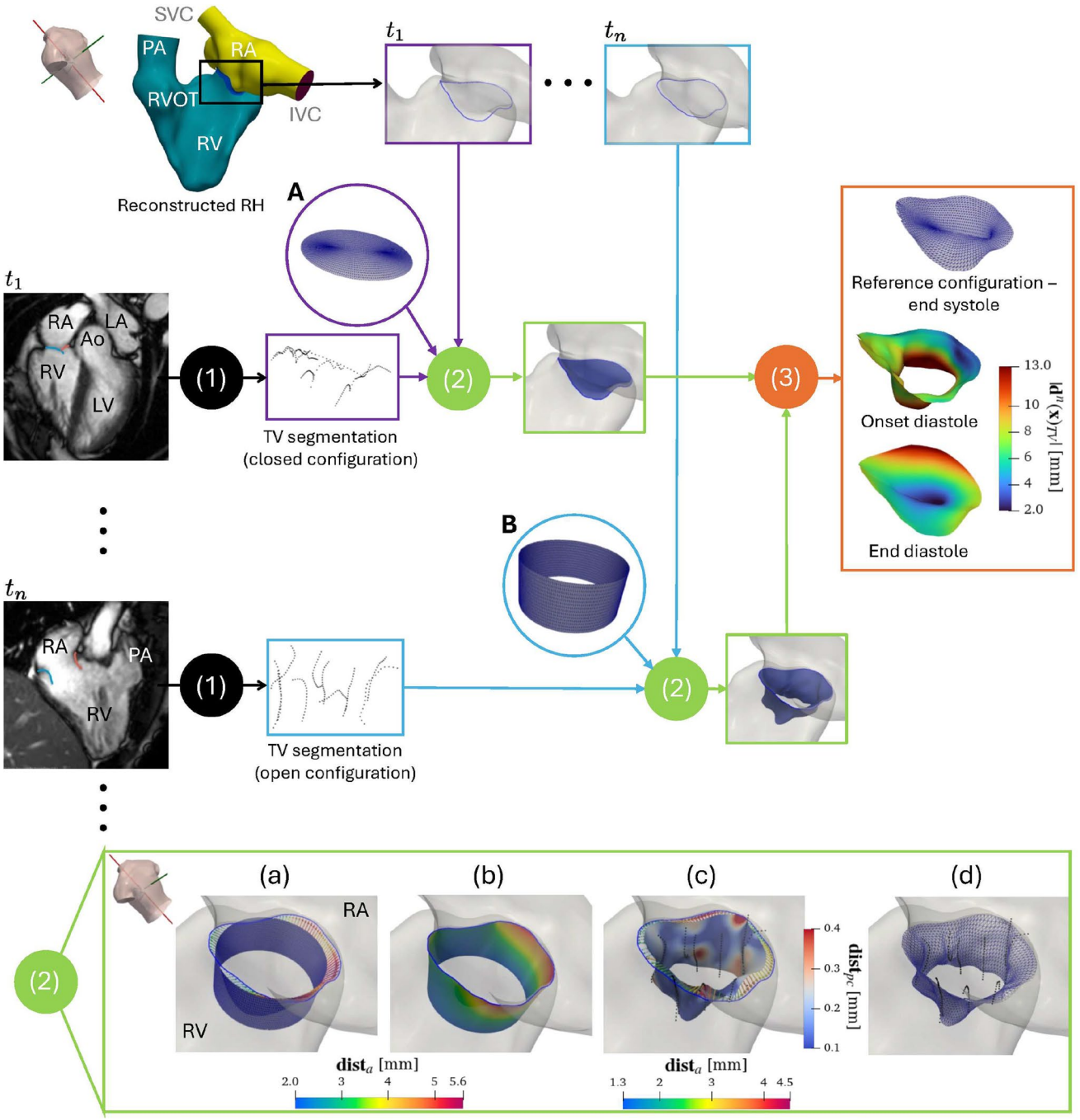

Fig. 2 Flowchart of the reconstruction procedure for the TV (Sect. 2.3) depicted at two representative instants: the onset diastole (light blue boxes and arrows) and end-diastole (purple boxes and arrows). Top row: extraction of the annulus from the RH geometry for all frames. Full circle (1): leaflets segmentation from cine MRI data for all frames. Circle panels A and B: representation of the template surfaces for recovering the closed and open TV configurations, respectively. Full circle (2): template morphing procedure. Full circle (3): TV displacement procedure. Orange box: representation of the TV mesh at the reference end-systolic configuration (top) and representation of the displacement field magnitude at the onset (middle) and at the end (bottom) of diastole. Bottom row—green panel, focus on one iteration of the template morphing procedure: **a** computation of the distance between the annulus border on RH and the annulus ring on the template, $\mathbf{dist}_a$; **b** representation of the extended $\mathbf{dist}_a$ on the template surface deformed accordingly; **c** representation of the extended distance field computed between the template surface output of (**b**) and the segmented point cloud (black dots), $\mathbf{dist}_{pc}$, on the template surface deformed accordingly. The newly computed $\mathbf{dist}_a$ field is represented too; **d** final result of the current iteration. Ao: aorta; IVC: inferior vena cava; LA: left atrium; LV: left ventricle; PA: pulmonary artery; RA: right atrium; RV: right ventricle; RVOT: right ventricle outflow tract; SVC: superior vena cava

2. The deformation of a template surface over the segmented TV;
3. The computation of the TV displacement field over the heartbeat.

For step 1 (see Fig. 2), we employ all the cine MRI series in which the valve is visible, in both the short- and long-axis views: For each time frame of these series, we manually trace the TV leaflets' profile. Since all the slices of the considered series have an in-plane spatial resolution ($\simeq 1.15 - 1.25$ mm) comparable with the thickness of the leaflets (about 1.5 mm), we believe that this method, unlike using only short-axis views, is able to properly reconstruct the valve orifice independently of its inclination (see Fig. 2). This step is accomplished by exploiting the Markups module of the open-source software 3D Slicer (https://www.slicer.org/). Then, we collect contours traced at the same frame together to obtain N separate point clouds, representing the segmentation of the subject's valve at each frame. We notice that these segmentations are highly sparse since the valve is usually visible in a small subset of the available cine MRI dataset.

Step 2 (depicted in the green panel of Fig. 2 for a diastolic frame) consists of (i) the inclusion of a template surface into RH endocardial reconstruction and (ii) the deformation over the TV segmentations, obtained in step 1, to retrieve the leaflet's morphology. In particular, to attain (i), we first compute the distance field between the TV annulus of the RH endocardium reconstruction and the closest border of the template. Then, we extend this distance field over the entire template surface and deform it accordingly. This allows us to connect the template surface to the TV annulus. After that, in (ii), we compute the pointwise distance between the connected surface and the TV point cloud, and we extend this field over the entire surface and warp it accordingly. In order to let the surface better resemble the segmented leaflet profiles, we iterate (ii) a few times (e.g., two or three). Finally, we repeat (i) to compensate for a possible surface detachment from the TV annulus and recover the connection. We observe that, as a template for step 2, we employ two different surfaces sharing the same connectivity: a disk to recover the TV closed configurations and a hole cylinder to recover the TV open configurations (see the purple circles in Fig. 2). Consequently, the connectivity is preserved among all the N TV surfaces, representing the valve's time evolution.

This feature is exploited in step 3 to trivially recover the TV displacement field. Namely, we compute the displacement of each configuration with respect to a reference one (e.g., at the end-systolic instant) by simply subtracting the node coordinates of their triangulations.

The outcome of the presented procedure is the triangulated TV surface at the reference frame together with the definition of its displacement fields $\mathbf{d}^n(\mathbf{x})$, $n = 1, \dots, N$. Figure 2, orange panel, shows the reference surface and magnitude of $\mathbf{d}^n(\mathbf{x})$ at two representative frames.

2.4 Reconstruction of pulmonary valve geometry and motion

In this work, we build the following healthy and repaired-ToF scenarios:

1. A healthy case, starting from the RH geometry of subject H;
2. A repaired-ToF with severe pulmonary regurgitation (PVReg-ToF), starting from the RH geometry of patient ToF;
3. A postoperative non-regurgitant scenario, obtained from case ii), by considering a virtual transcatheter PVR (PVnoReg-ToF).

To this aim, we introduce a procedure to include a competent pulmonary valve model in H and PVnoReg-ToF scenarios, and regurgitant pulmonary valve model in PVReg-ToF case. Since the cine MRI at our disposal does not allow a complete reconstruction of the patient-specific leaflets for any frame of the cardiac cycle, we employ the procedure followed by Bennati et al. (2023a). Specifically, we geometrically modify the PV geometry of the Zygote solid 3D heart model (representing the average PV leaflets of a healthy population, https://www.zygote.com) to match the reconstructed patient's annulus. This geometrical adaptation is achieved by exploiting closest point distance-based algorithms available in `vmtk` (Antiga et al. 2008; Fedele and Quarteroni 2021). Notice that this PV model is available in the fully closed configuration and includes a predefined displacement field to open the valve. By applying this displacement field, we are able to obtain the open configuration for the adapted model for H and PVnoReg-ToF scenarios.

In order to replicate the PV insufficiency for the PVReg-ToF scenario, we consider as closed configuration the one obtained by applying a percentage (50%) of the opening available displacement field. Such percentage is suitably selected to induce the same regurgitant fraction (RF) as the patient.

Finally, we recover the opening and closure PV dynamics by interpolating the adapted fully open and fully (or partially) closed configurations in time. This interpolation is, in practice, realized within the Finite Elements solver (see Sect. 2.5.1).

2.5 Dynamic image-based computational fluid dynamics model

2.5.1 Modeling details

Starting from the RH surfaces reconstructed as described in Sect. 2.2 at the end-systolic instant, we complete the

computational domain for the DIB-CFD models of the three scenarios introduced in Sect. 1 by including the reconstructed valves (see Sects. 2.3 and 2.4). We then generate a tetrahedral volumetric mesh.

To summarize, in each scenario, the reference RH mesh, together with its valves, defines our computational domain in the reference configuration $\hat{\Omega}$. Figure 3a illustrates DIB-CFD domain. Here, Γ_{TV} and Γ_{PV} are the surfaces representing the TV and PV's leaflets, respectively. By Σ_w, we denote the boundary comprising the ventricular and atrial endocardia and the pulmonary artery, IVC, and SVC walls. The outlet section of the pulmonary artery is indicated as Σ_{out}, and the inlet sections of IVC and SVC as Σ_{in}.

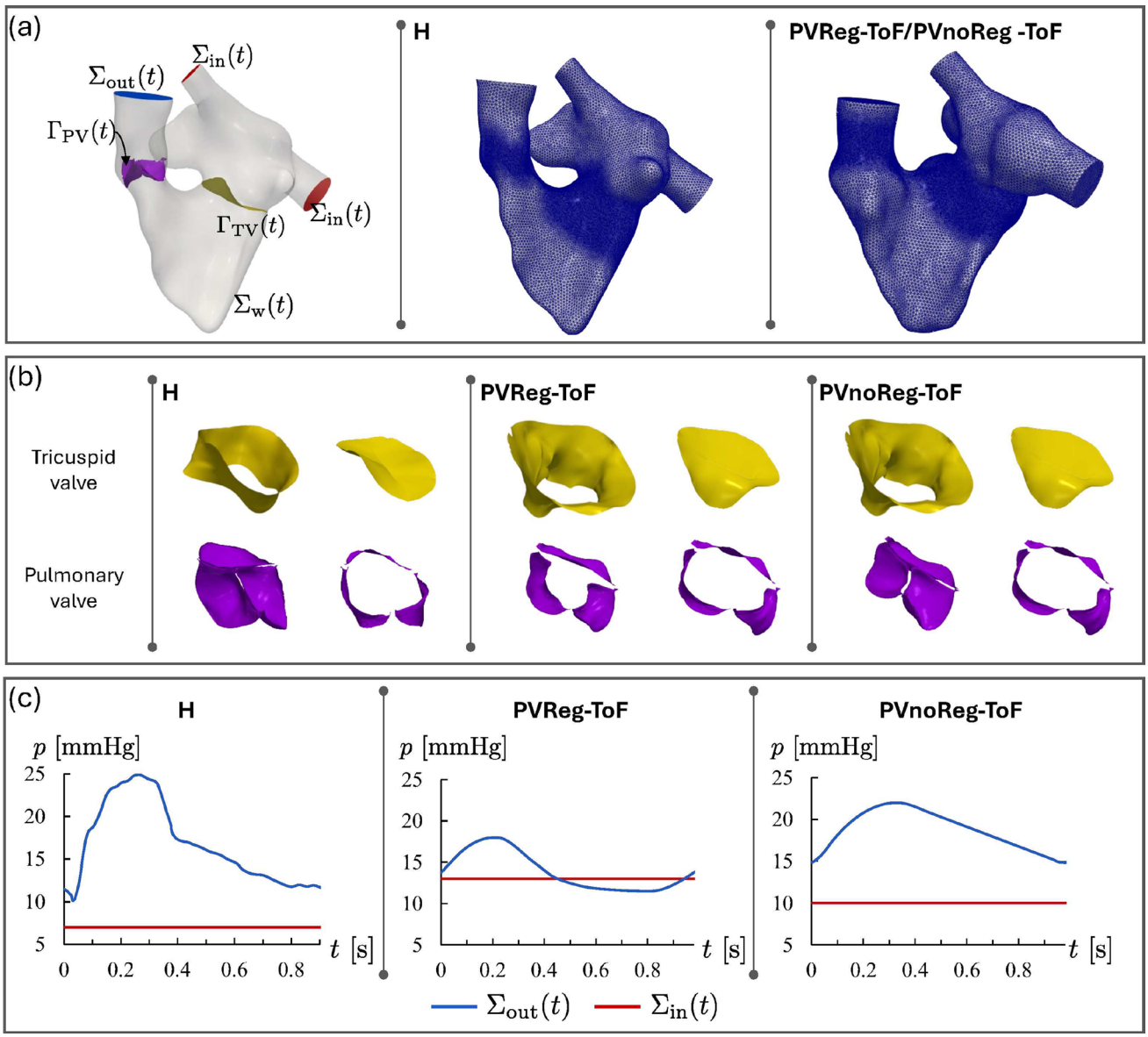

Fig. 3 Computational domains and boundary conditions. **a** On the left column the representation of the whole right heart $\Omega(t)$ with its boundaries showed only for the healthy (H) scenario: ventricle outflow $\Sigma_{out}(t)$ (blue); atrial inflows at the superior and inferior vena cava $\Sigma_{in}(t)$ (red); ventricular and atrial endocardium and physical wall of the pulmonary artery $\Sigma_w(t)$; surface of the pulmonary valve's leaflets $\Gamma_{PV}(t)$; surface of the tricuspid valve's leaflets $\Gamma_{TV}(t)$. On the central and right columns, RH tetrahedric volumetric mesh for the healthy subject (H) and the repaired-ToF patient (ToF), respectively. **b** Tricuspid and pulmonary valves in fully open and fully closed configurations for the healthy (H), the regurgitant repaired-ToF (PVReg-ToF), and the non-regurgitant repaired-ToF (PVnoReg-ToF) scenarios. **c** Pressure curves at the pulmonary artery (blue line) and inferior and superior vena cave (red line), imposed as boundary conditions; values for H come from the literature (Grignola 2011; Pappano and Wier 2018); values for PVReg-ToF and PVnoReg-ToF come from calibrated lumped parameter model (Criseo et al. 2024)

In what follows, we detail the mathematical model describing the blood flow and its interaction with the endocardium and valves in a moving setting.

We assume that blood behaved as an incompressible Newtonian fluid in heart chambers and large vessels (Quarteroni et al. 2019) with a density of $1.06 \cdot 10^3$ kg/m^3 and dynamic viscosity of $3.5 \cdot 10^{-3}$ Pa $\cdot$ s. Therefore, we consider the Navier–Stokes equations in a moving domain. As described in Sect. 2.2, the displacement $\mathbf{D}^n(\mathbf{x})$ of the domain $\Omega(t)$ with respect to its reference configuration $\widehat{\Omega}$ was reconstructed from cine MRI only for the acquired N frames. Hence, we interpolate it in time with splines to cover the whole heartbeat duration. This leads to the definition of $\mathbf{D}(\mathbf{x}, t)$ for all $t \in [0, T]$ where T indicates the subject's heartbeat duration. $\mathbf{D}(\mathbf{x}, t)$ is then used to compute the wall velocity to prescribe to the fluid problem that is solved in an arbitrary Lagrangian–Eulerian (ALE) formulation (Hirt et al. 1997; Nobile and Formaggia 1999). According to this framework, at each t, $\mathbf{D}(\mathbf{x}, t)$ (which is defined on Σ_w) is extended within $\widehat{\Omega}$ by solving a Linear Elasticity problem (Stein et al. 2003). See Africa et al. (2024) and Renzi et al. (2025) for further details on the used solver. To account for possible transition to turbulence, we consider the large eddy simulation σ model (Nicoud et al. 2011). Regarding the valves, we model them as thick surfaces immersed in the fluid dynamics domain without relying on fluid–structure interaction modeling. In particular, their presence is managed by the Resistive Immersed Implicit Surface (RIIS) method (Fernández et al. 2008; Fedele et al. 2017; This et al. 2020). We handle differently the valve dynamics in the cases of TV and PV. For the TV motion, we linearly interpolate over the heartbeat duration the reconstructed displacement field $\mathbf{d}^n(\mathbf{x})$ (Sect. 2.3). Instead, the PV motion is achieved by prescribing opening and closing intervals by images (Fumagalli et al. 2020). The valve dynamics is handled by a cosine interpolation between the fully closed and fully open valve configurations.

2.5.2 Details on the meshes

As illustrated in Fig. 3, we build tetrahedral meshes of the RH cavity with heterogeneous size h for the healthy (H) and for the repaired-ToF (ToF) cases, exploiting the `vmtk` meshing tools. The ToF mesh is used in both the PVReg-ToF and PVnoReg-ToF scenarios. We refine further the mesh element size in the regions occupied by TV and PV during their motion. This refinement is done up to half the leaflets' thickness (we assume a constant thickness throughout the leaflets equal to 1.5mm) in order to correctly represent the valves using the RIIS method. Notice that we do not need to build any mesh for the leaflets' valves as they are treated as immersed surfaces according to the RIIS method (Fedele et al. 2017). Details about the constructed meshes are reported in Table 1.

2.5.3 Setup of numerical simulation

From the numerical standpoint, we discretize the DIB-CFD problem in space by adopting inf–sup stabilized $\mathbb{P}1 - \mathbb{P}1$ finite elements and a SUPG stabilization for advection-dominated flows (Tezduyar and Senga 2006). In time, we employ a semi-implicit backward Euler scheme with $\Delta t = 5 \times 10^{-4}$s. This time step and the mesh size (reported in Table 1) are selected upon conducting a convergence test as in Bennati et al. (2023a): finer meshes or smaller time steps do not yield significant differences in the results.

We simulated 7 heartbeats with period T equal to $0.91s$ and $0.96s$ for H and ToF, respectively, starting from a null initial condition. Finally, we prescribe pressure curves, which are reported in Fig. 3, as boundary conditions at the inlets Σ_{in} and the outlet Σ_{out}. Specifically, physiological pressures for H scenario are taken from Pappano and Wier (2018), while pathological pressure curves for PVReg-ToF and PVnoReg-ToF scenarios are obtained from a calibrated lumped parameter model (details can be found in Criseo et al. 2024). The latter are consistent with findings of pulmonary regurgitant and postoperative ToF patients reported in the literature (Egbe et al. 2019; Abozied et al. 2024). Notice that we assume, for the sake of simplicity, constant-in-time pressures for IVC and SVC, since variations in time during normal respiration are very small (Scott 1963).

We solve numerically the fluid dynamics problem in the moving domains described in Sect. 2.5.1 and simulate: the healthy (H), the (pulmonary) regurgitant repaired-ToF (PVReg-ToF), and the postoperative non-regurgitant repaired-ToF (PVnoReg-ToF) scenarios. The simulations are executed in `life`^{x} (Africa 2022; Africa et al. 2024) (Finite Element, FE, C++ library based on `deal.II`, Arndt et al. 2022, FE core and developed at MOX, Politecnico

Table 1 Details about the tetrahedral meshes used for the DIB-CFD simulations

Patient	H	PVReg-ToF/ PVnoReg-ToF
Number of cells	3, 927, 369	2, 169, 648
Total DOFs	2, 578, 280	1, 462, 132
$h_k^{\max}$ [mm]	3.83	3.88
h_k^{mean} [mm]	0.85	0.99
$h_k^{\min}$ [mm]	0.32	0.32

Total DOFs include both pressure and velocity DOFs and refer to linear finite elements

di Milano, within the framework of the iHEART project https://iheart.polimi.it) and carried out using 144 parallel processes on the Tier-0 EuroHPC supercomputer LEONARDO (hosted by Cineca high-performance computing center https://www.hpc.cineca.it, Bologna, Italy).

2.6 Computation of post-processed quantities

We compute the quantity of interest discarding the first heartbeat to remove the unphysical influence of the initial null solution. In particular, we observe that the numerical solution stabilizes thereafter, with variations below 1%, justifying the removal of only one heartbeat.

To analyze the overall topology of the flow field, we consider the ensemble blood velocity and pressure defined as follows:

$$\langle \mathbf{u}(\mathbf{x},t)\rangle = \frac{1}{N_{\mathrm{HB}}}\sum_{n=1}^{N_{\mathrm{HB}}} \mathbf{u}(\mathbf{x},t+(n-1)T),$$

$$\langle p(\mathbf{x},t)\rangle = \frac{1}{N_{\mathrm{HB}}}\sum_{n=1}^{N_{\mathrm{HB}}} p(\mathbf{x},t+(n-1)T),$$

where $\mathbf{u}$ and p are the instantaneous blood velocity and pressures, while N_{HB} refers to the total number of simulated heartbeats discarding the first one. We indicate with the symbol $\langle\cdot\rangle$ the average over N_{HB} heartbeats of period T. We compute the velocity fluctuation field $\mathbf{u}'$ by adopting the Reynolds decomposition (Pope 2001) $\mathbf{u} = \langle\mathbf{u}\rangle - \mathbf{u}'$, and we analyze:

- The Reynolds number (Yoganathan et al. 1988) across TV and PV, computed as:

  $$\mathrm{Re} = \frac{\rho \bar{V} D}{\mu},$$

  where ρ and μ are the blood density and molecular viscosity, respectively. We indicated with D the diameter of the equivalent circle area of the valve orifice and with $\bar{V}$ the cross-sectional fluid velocity obtained by spatially averaging the total flow over the valve orifice area;
- The root mean square and the standard deviation of the velocity fluctuations indicated as u'_{rms} and $\boldsymbol{\sigma}$, respectively, and defined as (Pope 2001):

  $$u'_{\mathrm{rms}} = \sqrt{\langle u'_x\rangle^2 + \langle u'_y\rangle^2 + \langle u'_z\rangle^2},$$

  $$\sigma_i = \sqrt{\langle u'_i\rangle^2} \qquad \text{with } i = x,y,z.$$

  These allow us to quantify and localize the velocity fluctuations among the heartbeats;
- The total mean kinetic energy (MKE) and the total turbulent kinetic energy:

  $$\mathrm{MKE} = \rho\int_\Omega \frac{1}{2}\|\langle\mathbf{u}\rangle\|^2,$$

  $$\mathrm{TKE} = \rho\int_\Omega \frac{1}{2}u'^2_{\mathrm{rms}},$$

  where $||\cdot||$ indicates the Euclidean norm. In particular, TKE allows to identify the temporal instants where velocity fluctuations are more pronounced (Pope 2001);
- The turbulence intensity (TI) (Yoganathan et al. 1988; Pope 2001):

  $$\mathrm{TI} = \frac{\mathrm{TKE}}{\mathrm{MKE}}\%,$$

  which measures the global strength of turbulence in the flow.

Finally, to quantify the stresses on the wall exerted by the blood flow and the possible presence of blood stagnation regions near the endocardium, we compute the following quantities derived from the ensemble velocity (Riccardello Jr et al. 2018; Bennati et al. 2023a):

- The wall shear stress (WSS), defined as (Katritsis et al. 2007):

  $$\mathrm{WSS}(\mathbf{x},t) = \mathbf{Tn} - (\mathbf{Tn})\cdot\mathbf{n},$$

  where $\mathbf{T}$ is the fluid Cauchy stress tensor and $\mathbf{n}$ is the normal versor;
- The time average wall shear stress (TAWSS), computed as:

  $$\mathrm{TAWSS}(\mathbf{x}) = \int_0^T \mathrm{WSS}\,\mathrm{d}t;$$

- The relative residence time (RRT), computed as (Himburg et al. 2004):

  $$\mathrm{RRT}(\mathbf{x}) = \frac{1}{(1-2\mathrm{OSI}(\mathbf{x}))\mathrm{TAWSS}(\mathbf{x})},$$

  where *OSI* indicates the oscillatory shear index which is defined as:

  $$\mathrm{OSI}(\mathbf{x}) = \frac{\|\int_0^T \mathrm{WSS}(\mathbf{x},t)\mathrm{d}t\|}{\int_0^T \|\mathrm{WSS}(\mathbf{x},t)\|\mathrm{d}t}.$$

3 Reconstruction results

In this section, we focus on the reconstruction results obtained by exploiting the MSMorph technique (Renzi et al. 2025) and the procedures described in Sects. 2.3 and 2.4 for the RH and the TV and PV valves, respectively.

In Table 2, we report the indexed RV and RA volumes. Notice that for the healthy case H such values fall down in physiological ranges, i.e., $54 - 122\,\mathrm{ml/m^2}$ for the RV V_{max}, $16 - 60\,\mathrm{ml/m^2}$ for RV V_{min}, $9 - 45\,\mathrm{ml/m^2}$ for RA V_{min}, and $28 - 76\,\mathrm{ml/m^2}$ for RA V_{max}, see Renzi et al. (2025) and reference and Table 2 therein. Notice also that PVReg-ToF/PVnoReg-ToF is instead severely dilated, with, however, no evidence of tricuspid regurgitation. Differences in terms of morphology is qualitatively shown in Fig. 4, left column, which depicts H and PVReg-ToF/PVnoReg-ToF's RH in the reference end-systolic configuration. Regarding wall dynamics, we observe a relevant displacement of the intraventricular septum at the end of diastole in PVReg-ToF/PVnoReg-ToF as compared to the control (see Fig. 4 middle column). Further alterations of the PVReg-ToF/PVnoReg-ToF RH dynamics are revealed by the atrial and ventricular volume trends shown in Fig. 4, left column. Specifically, the PVReg-ToF/PVnoReg-ToF RA is characterized by a poor contraction and its contribution to the ventricular diastolic filling due to the atrial kick is almost absent. As a consequence, we observe a prolonged ventricular diastasis.

Concerning valves, Fig. 3b depicts the reconstructed TV for both subjects in the fully closed and open configurations. In order to qualitatively assess the fidelity to the image, Fig. 5 presents the superposition of these results on four-chamber and right ventricle outflow tract (RVOT) cine MRI planes. Values of TV orifice area (TOA) at the diastolic E-wave and A-wave instants are provided in Table 3 together with the values of the PV orifice area (POA) at the peak systolic instant. These quantities are

Table 2 Patients' volumetric indexes

Patient	BSA (m^2)	RV V_{max} (ml/m^2)	RV V_{min} (ml/m^2)	RA V_{min} (ml/m^2)	RA V_{max} (ml/m^2)
H	1.96	100.6	59.2	37.2	61.0
PVReg-ToF/ PVnoReg-ToF	1.25	178.9	113.5	52.2	63.6

BSA = body surface area; RV V_{max} (ml/m^2) = indexed right ventricle maximum volume reached during diastole; RV V_{min} (ml/m^2) = indexed right ventricle minimum volume reached during systole; RA V_{min} (ml/m^2) = indexed right atrium minimum volume reached in diastole; RA V_{max} (ml/m^2) = indexed right atrium maximum volume reached in systole

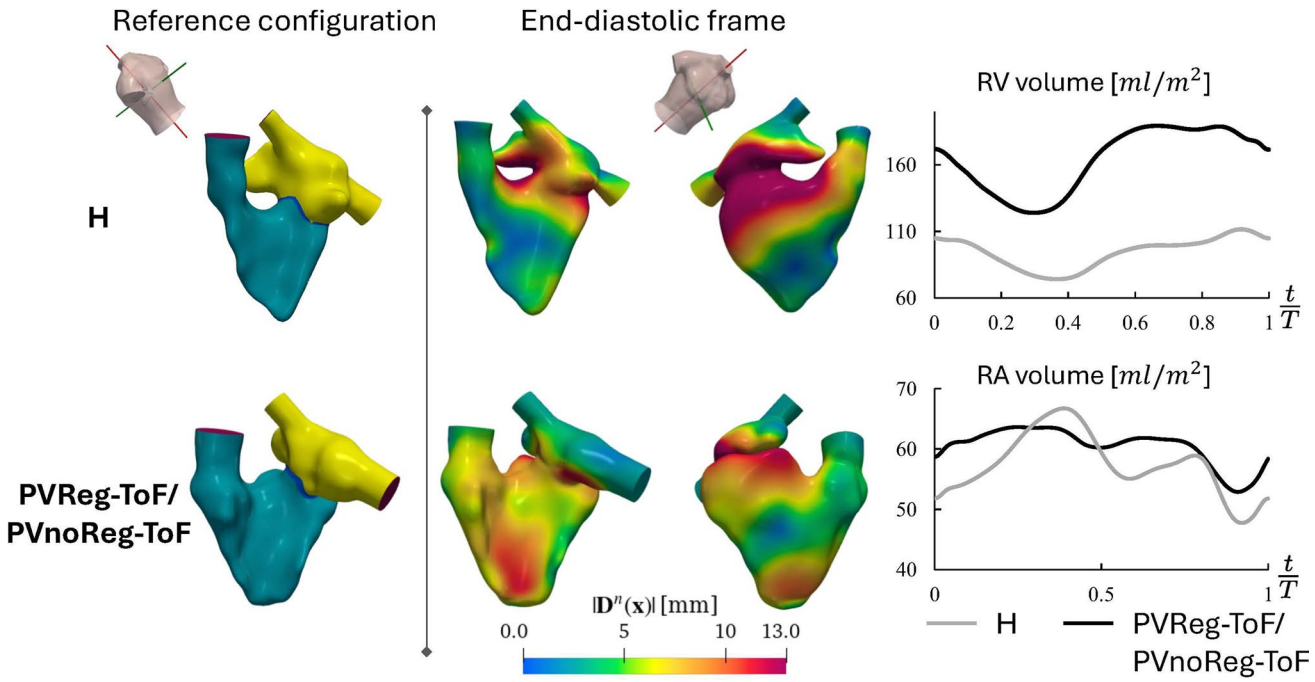

Fig. 4 Reconstructions of the RH in the reference configuration and displacement fields for the healthy (H) and repaired-ToF (PVReg-ToF/PVnoReg-ToF) subjects. On the left column, reference configurations at end-systole with region tags: yellow—right atrium; blue—TV annulus; turquoise green—right ventricle; red—inflow and outflow sections. On the middle column, magnitude of $\mathbf{D}^n$ at end-diastole in the corresponding geometrical configuration. On the right column, ventricular and atrial volume curve over time for both subjects. Times are normalized w.r.t. the subject's heartbeat period

calculated in post-processing as the area enclosed by the valve at the plane of the leaflet free margins.

The results of adapting the Zygote template PV to the subjects' annulus are shown in Fig. 3b for both the PVReg-ToF and PVnoReg-ToF scenarios. In particular, we recall that to simulate the patient regurgitant fraction (RF) in the PVReg-ToF scenario, we further modify the PV template by leaving a gap between the leaflet's free margins (see Sect. 2.4). Specifically, to replicate the patient's RF = 38%, we apply 50% of the opening displacement defined on the adapted Zygote template, which leads to a pulmonary regurgitant area of about 2.42 cm^2. For H and PVReg-ToF scenarios, the mean PV opening velocities are 248 mm/s and 168 mm/s, respectively. The value for the healthy case is consistent with literature values reported by Nanda et al. (1974). However, to the best of the authors' knowledge, reference values for regurgitant pulmonary valves are not currently available. In the PVnoReg-ToF scenario, the mean pulmonary valve opening velocity was about 430 mm/s, which seems slightly higher than the normal ranges. In addition, Table 3 reports the normalized times indicating the onset of TV opening and closing (PV opening and closing, respectively). Fully TV closure is reached at the end of the heartbeat for both subjects.

4 Numerical results

In this section, we present the results of the DIB-CFD analysis in the three scenarios presented in Sect. 1, namely a healthy control (H), a repaired-ToF with severe pulmonary regurgitation (PVReg-ToF), and a postoperative non-regurgitant repaired-ToF (PVnoReg-ToF).

4.1 Characterization of flow and pressure fields

In this section, we report and describe the ensemble velocity field $\langle \mathbf{u} \rangle$, the flows across the pulmonary and tricuspid valves, and the global mean kinetic energy (MKE) for the RA and RV.

The maximum ensemble velocities and flows through valves are reported in Table 4 for the three scenarios at three relevant instants: peak systole and peak diastolic E-wave and A-wave. In all three cases, the pulmonary jet during systole was characterized by maximum velocity values at the pulmonary valve orifice comparable to physiological 4D flow measurements available in the literature (Hudani et al. 2023; François et al. 2012). Regarding the blood velocity through TV, we observe that for H it is within the physiological ranges (< 0.7 m/s), while PVReg-ToF and PVnoReg-ToF show an increased value which is classifiable as mild stenotic (Baumgartner et al. 2009). A suspect of mild TV

Table 3 Characterization of tricuspid (TV) and pulmonary (PV) valves

Patient	TOA_{Ew} (cm^2)	TOA_{Aw} (cm^2)	POA (cm^2)	t_o/T	t_c/T	HR (bpm)
H	10.10 (5.15)	6.35 (3.24)	5.32 (2.71)	0.36	0.92	64
PVReg-ToF	4.36 (3.49)	3.12 (2.50)	5.84 (4.67)	0.34	0.87	60
PVnoReg-ToF						

TOA_{Ew} and TOA_{Aw} indicate the tricuspid orifice area at the E-wave and A-wave instants, respectively; *POA* indicates the pulmonary orifice area; in brackets the values normalized with respect to BSA. t_o/T and t_c/T correspond to the normalized times of the onset of TV opening and closing (PV closing and opening, respectively), respectively, expressed as a fraction of the subject's heartbeat duration. HR: Heart Rate

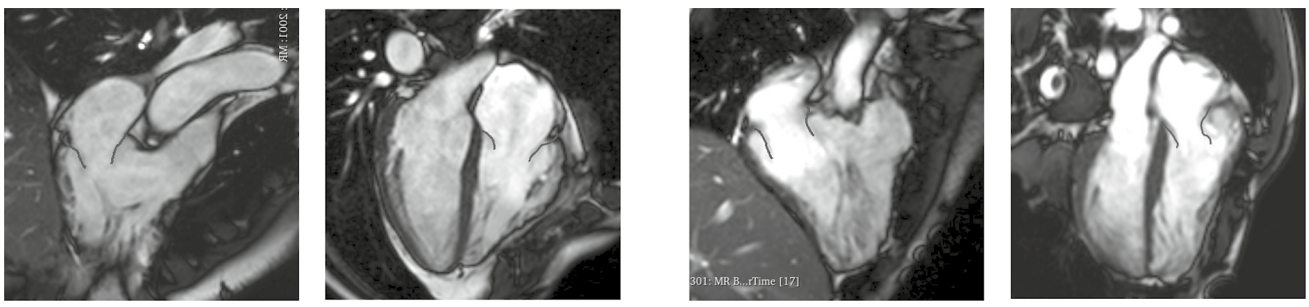

Fig. 5 Intersection of the reconstructed TV surfaces (green line) with the cine MRI planes for the healthy subject (**a** and **b**) and the repaired-ToF patient (**c** and **d**). Images **a** and **c**: RV inflow views; images **b** and **d**: four-chamber views. Notice that **c** and **d** are taken at the maximum diastolic TV opening frame, highlighting the mild TV stenosis

Table 4 Magnitude of the ensemble velocity $\langle \mathbf{u} \rangle$ and values of maximum flows Q at three instants: t_{ps} indicates peak systole; t_{Ew} and t_{Aw} indicate peak E-wave and A-wave, respectively

Scenario	$\|\langle \mathbf{u} \rangle\|_{ps}$ (m/s)	$\|\langle \mathbf{u} \rangle\|_{Ew}$ (m/s)	$\|\langle \mathbf{u} \rangle\|_{Aw}$ (m/s)
H	1.0	0.4	0.4
PVReg-ToF	1.1	1.0	0.7
PVnoReg-ToF	1.3	1.9	0.7
	Q_{ps}^{PV} (ml/s · m^2)	Q_{Ew}^{TV} (ml/s · m^2)	Q_{Aw}^{TV} (ml/s · m^2)
H	156.7	136.4	97.0
PVReg-ToF	248.7	242.8	54.6
PVnoReg-ToF	248.2	378.8	46.0
	TRV (ml/m^2)	Δp_{Ew} (mmHg)	Δp_{Aw} (mmHg)
H	5.9	1.0	1.0
PVReg-ToF	5.9	2.8	0.9
PVnoReg-ToF	16.9	6.5	1.2

TRV indicates the Tricuspid Regurgitant Volume. Flow values are normalized w.r.t the patients' BSA. Average pressure drop Δp across the tricuspid valve during E-wave (Ew) and A-wave (Aw) diastolic phases for the three simulated scenarios. TV = tricuspid valve; PV = pulmonary valve

stenosis could be inferred by the values of the normalized *TOA* reported in brackets in Table 3. Notice that, although stenosis of TV is a quite rare condition, a few cases of ToF patients affected by such condition have been reported in the literature (Lev and Eckner 1964; Litovsky et al. 2000).

Table 4 reports also the blood pressure drop across TV. H exhibits a pressure drop of about 1 mmHg during diastole, while PVReg-ToF and PVnoReg-ToF showed an average value of about 3 and 6 mmHg, respectively, during the E-wave. During A-wave, both PVReg-ToF and PVnoReg-ToF had an average TV pressure drop of about 1 mmHg. Figure 6 illustrates the time trends of pulmonary and tricuspid flows throughout the cardiac cycle together with 3D representations of the ensemble velocity magnitude. Regarding the reported flows, they correspond to the time derivative of the volume curves presented in Fig. 4, which are obtained by interpolating the available endocardial configurations reconstructed for each cine MRI frame (Sect. 2.2). Notice that a (probably) non-physiological behavior of the pulmonary flow rate could be seen at the beginning of systole in the PVReg-ToF and PVnoReg-ToF scenarios, likely due to the effect of the interpolation between two consecutive cine MRI acquisition frames.

Examining the velocity magnitude, we notably observed that, in the H case, the flow entering the RV through TV during the early diastole did not extend into the apical region. This behavior was further highlighted by the flow streamlines depicted in Fig. 7. In addition, we detected a separation among the inward flows from the inferior vena cava (IVC) and the superior vena cava (SVC), persisting throughout most of the diastole. Specifically, the blood coming from IVC impinged on the RV anterior wall and then flowed mainly toward the RVOT. At the same time, blood flow from SVC moved deeper toward the ventricular apex without reaching it and drifted upwards behind the tricuspid leaflets. In the PVReg-ToF and PVnoReg-ToF cases, at the peak E-wave instant, a similar division of the flows from SVC and IVC was present (see arrows in Fig. 7). However, in the PVReg-ToF scenarios, the flow from IVC reached the ventricular apex, while the blood from SVC, after impinging on the anterior wall, deflected upwards. Both PVReg-ToF and PVnoReg-ToF exhibited high velocities within the tricuspid orifice in diastole. Moreover, TV leaflets oriented the high-velocity tricuspid jet toward a region of the anterior wall closer to the posterior wall.

Concerning the pulmonary regurgitation in the PVReg-ToF scenario, a counter-rotatory flow coming from the pulmonary artery was present and acted as a barrier that prevented the tricuspid flow from reaching the RVOT (see pink arrow in Fig. 7). The peak pulmonary regurgitation occurred at 40% of the heartbeat and was characterized by a maximum flow of 149.6 ml/s · m^2 with a maximum velocity of 1.7 m/s. Moreover, looking at the ensemble pressure field shown in Fig. 8, we detected a relevant pressure drop below PV around which the pulmonary regurgitation inflow recirculates. High pulmonary regurgitant blood velocities persisted throughout the E-wave phase, reaching values of about 1.3 m/s at peak E-wave instant. Inversion of the regurgitant flow direction happened during the late diastole, with blood velocity approximately 0.18 m/s at peak A-wave. Also, the RV flow streamlines became more disorganized in this phase (see Fig. 7).

In the PVnoReg-ToF case, given that it shares the same wall displacement as PVReg-ToF, the presence of a

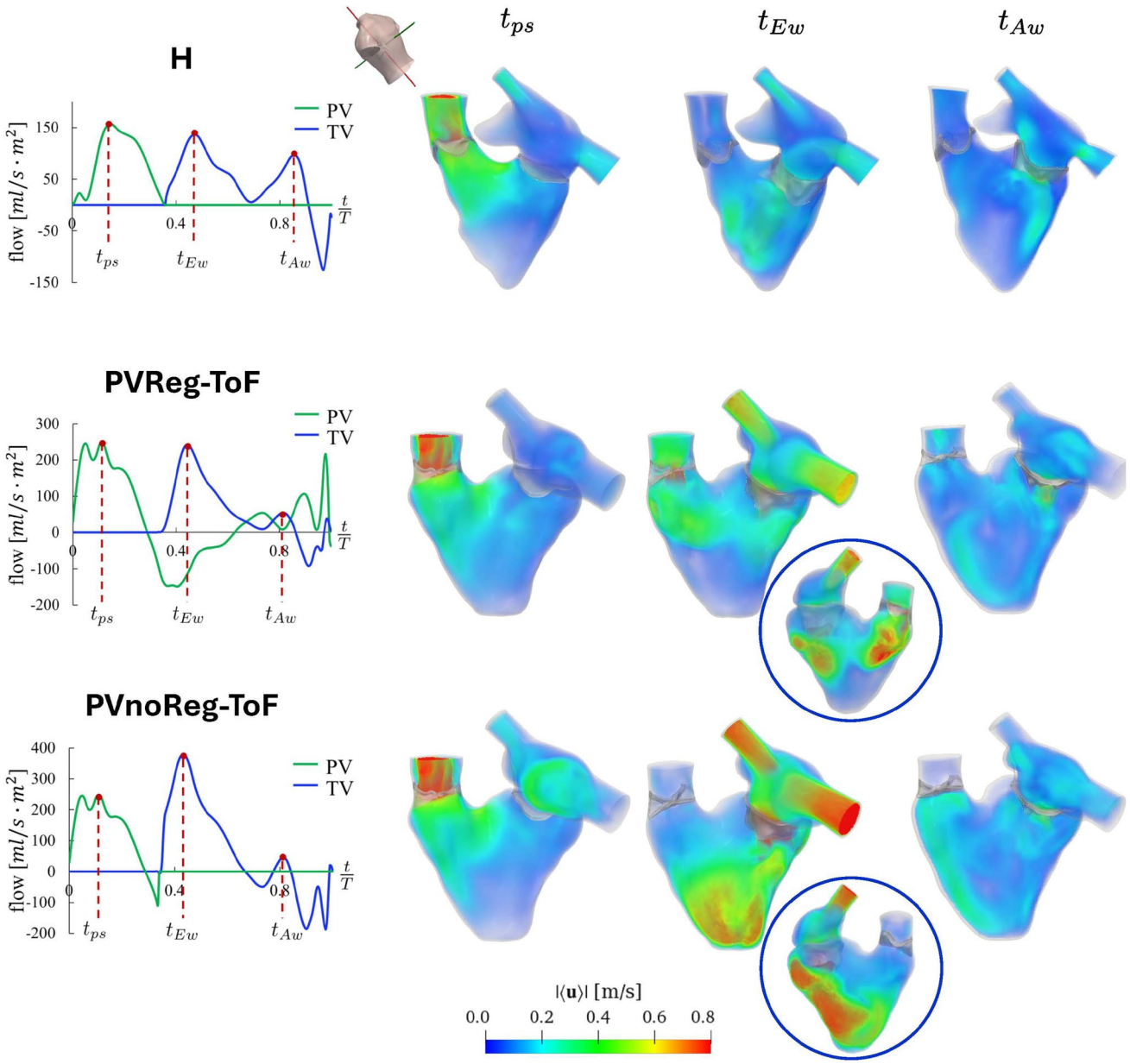

Fig. 6 Valves' flows and ensemble velocity magnitude for the three simulated scenarios: the healthy control (H), the repaired-ToF with severe pulmonary regurgitantion (PVReg-ToF), and the postoperative non-regurgitant repaired-ToF (PVnoReg-ToF). On the left columns, trends of flows through the pulmonary (PV) and the tricuspid valve (TV), with indication of three relevant frames: ps indicate the peak systole; Ew indicates the peak E-wave in early diastole; Aw indicates the peak A-wave in late diastole. On the right, the volume rendering of the ensemble velocity magnitude at the same instants. Blue circles: RH anterior view focusing on the jet impingement regions

competent PV causes a relevant depression within RV in diastole (see Fig. 8) leading to a significant increase of tricuspid flow (see Table 4). Similar negative diastolic pressure values (up to about −20 mmHg, see also Fig. 9) are commonly found immediately after pulmonary valve intervention, as reported in Mohr et al. (1986). Consequently to the negative ventricular pressure, the tricuspid jet impingement region on the anterior wall extended to the ventricular apex (see Fig. 6), and in the absence of a reentering pulmonary flow, the tricuspid flow was able to directly reach the RVOT (see white arrow in Fig. 7).

Ventricular pressure–volume (where for the volume we use the indexed quantity to facilitate comparisons among the cases) loops (P–V loops) are depicted in Fig. 9 for the three scenarios. Remember that pressure values are computed from our simulations while the volume values are obtained from the processing of cine MRI, thus explaining some oscillations due to noise in such curves. These

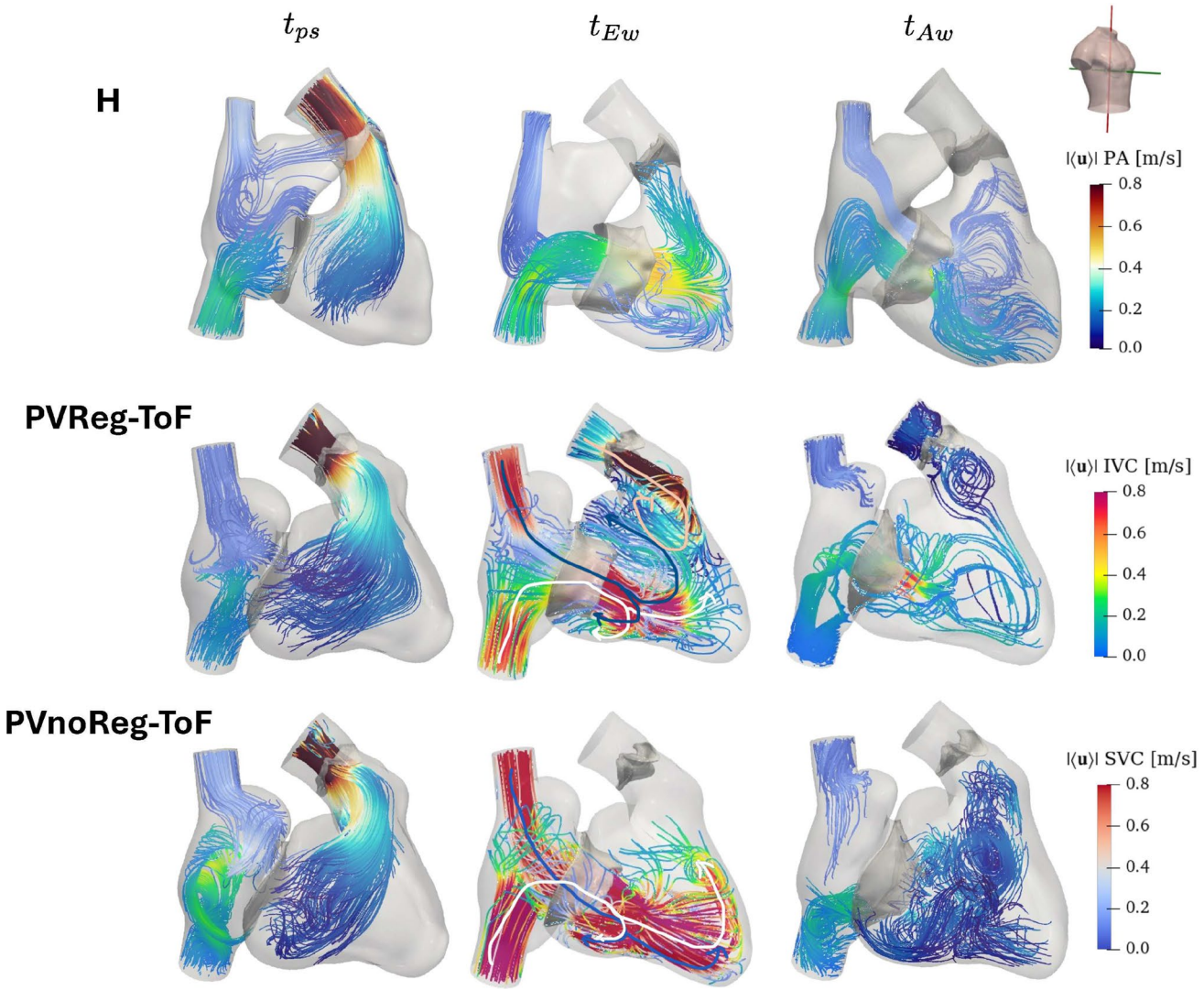

Fig. 7 Streamlines at three instants (peak systole t_{ps}, peak E-wave t_{Ew}, and peak A-wave t_{Aw}) for the three simulated scenarios: the healthy control (H), the repaired-ToF with severe pulmonary regurgitation (PVReg-ToF), and the postoperative non-regurgitant repaired-ToF (PVnoReg-ToF). Different color bars are used to indicate flows from the pulmonary artery (PA), inferior vena cava (IVC), and superior vena cava (SVC). Arrows indicate the main direction of flows: pink for the blood flow from PA; blue for the blood flow from SVC; white for the blood flow from IVC

results are in agreement with pressure values reported in Das et al. (2010). They also proved the absence of isovolumic relaxation in PVReg-ToF due to PV regurgitation, as well as reduced ventricular contractility with respect to the control case, reflecting literature findings (Das et al. 2010).

Finally, for PVReg-ToF scenario, Fig. 10 shows a comparison of the velocity field on the plane depicted in the figure for three representative instants between in vivo PC-MRI data and our numerical results. Notice in particular the inversion of flow in t_2 and the regurgitation at t_3 characterized by negative values. We observe an excellent agreement both quantitatively and in terms of pattern.

4.2 Analysis of transition to turbulence

For the analysis of the transition to turbulence within the RH, we reported the following quantities, which are defined in Sect. 2.6: In Table 5, the Reynolds numbers of the flows across PV and TV; in Fig. 11, the time trends of the global mean kinetic energy (MKE) together with the time trends of the global turbulent kinetic energy (TKE) and of the turbulence intensity (TI); in Fig. 12, the velocity fluctuation field u'_{rms} and the standard deviation of the velocity fluctuations $\boldsymbol{\sigma}$; in Fig. 13, the ratio between the sub-grid-scale and the

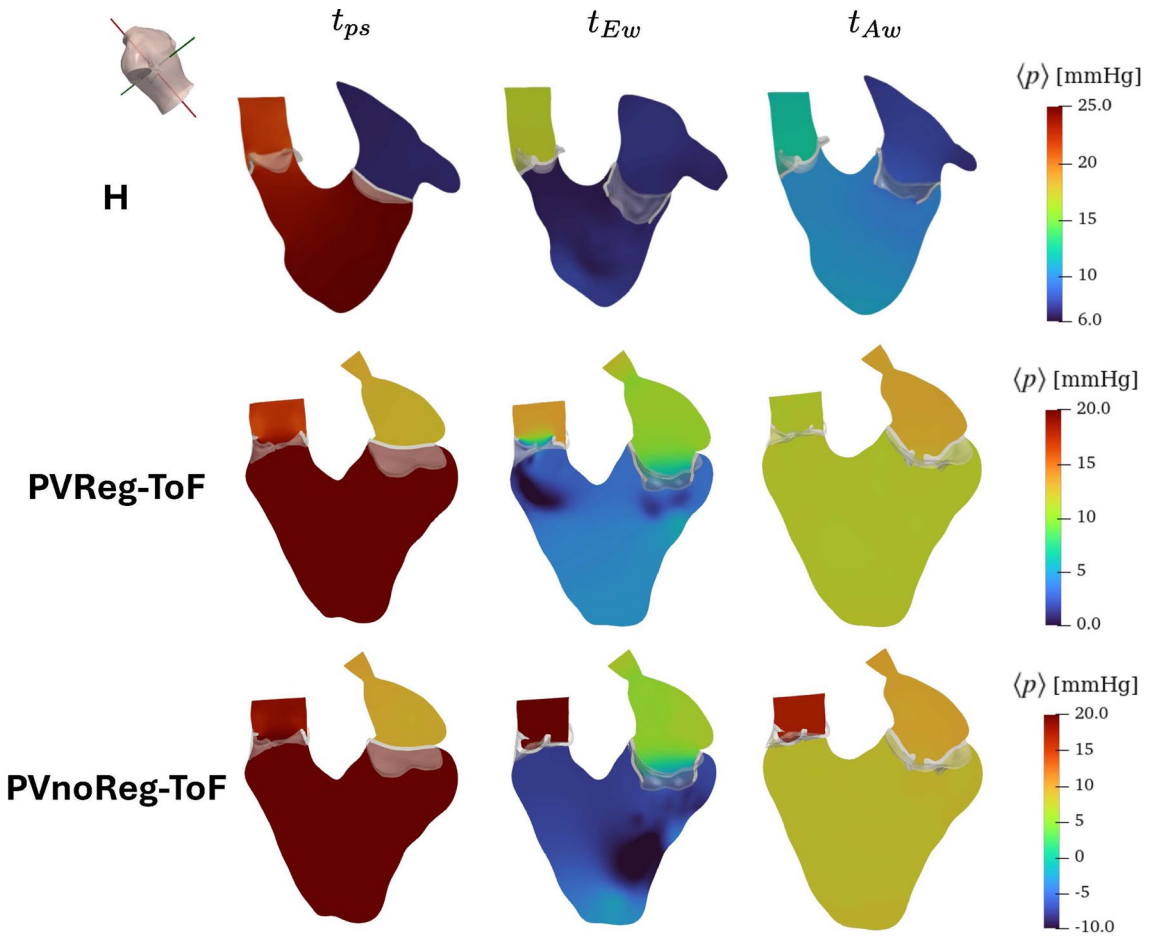

Fig. 8 Ensemble pressure for the three simulated scenarios: the healthy control (H), the repaired-ToF with severe pulmonary regurgitantion (PVReg-ToF), and the postoperative non-regurgitant repaired-ToF (PVnoReg-ToF). t_{ps} indicate the peak systolic instant; t_{Ew} indicates the peak E-wave instant in early diastole; t_{Aw} indicates the peak A-wave instant in late diastole

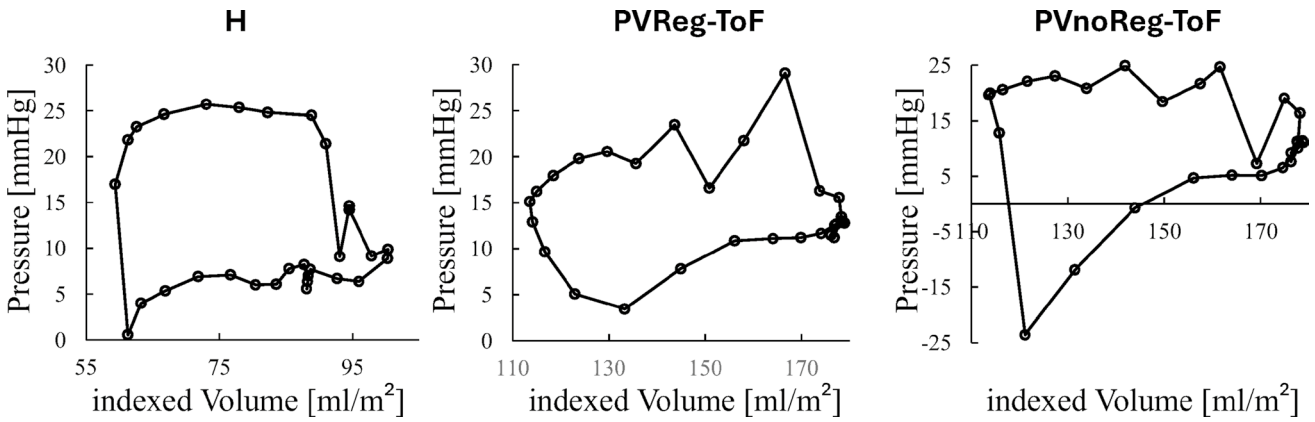

Fig. 9 Ventricular pressure-indexed volume loops for the three simulated scenarios: the healthy control (H), the repaired-ToF with severe pulmonary regurgitation (PVReg-ToF), and the postoperative non-regurgitant repaired-ToF (PVnoReg-ToF)

molecular viscosities, μ_{sgs}/μ, and the vorticity isosurfaces; and finally, in Fig. 13, we also show the percentage of volume subjected by $|\sigma| > 0.1$ m/s over the cardiac cycle.

Regarding MKE (Fig. 11) within RV, the typical three-peak curve (Barker et al. 2019) characterized all scenarios. Within RA, we observed that the MKE peak during early

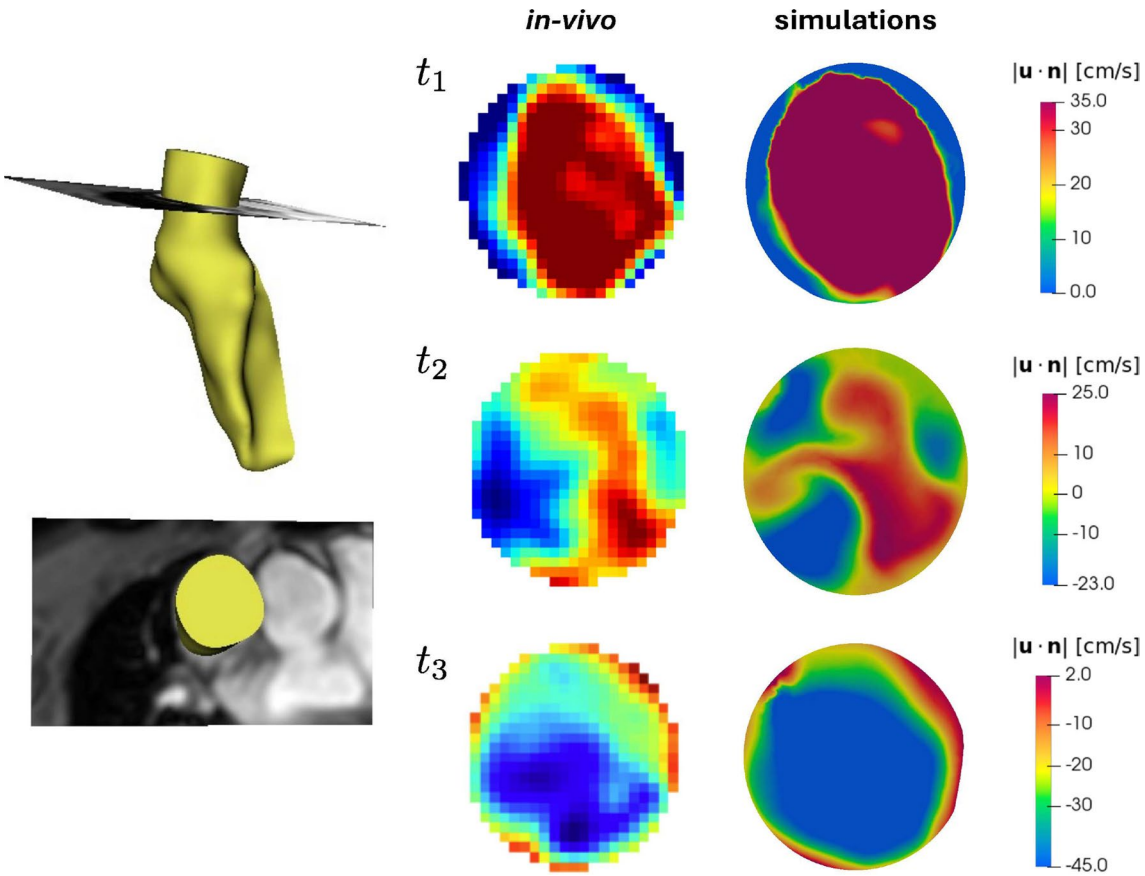

Fig. 10 Normal component of the velocity field on a section at the level of the pulmonary valve outflow tract (depicted on the left) obtained from PC-MRI data (in vivo column) and from numerical simulations (right column). Repaired-ToF patient with pulmonary regurgitation (PVReg-ToF). Three instants are considered: $t_1 = 0.32$ s corresponds to peak systole; $t_2 = 0.48$ s corresponds to a mid-instant of the descending phase of systole; $t_3 = 0.82$ s corresponds to the instant of peak regurgitant flow. Positive values mean blood flow going toward the lung, negative values mean blood flow coming back to the right ventricle

diastole is more pronounced in PVReg-ToF and PVnoReg-ToF. This is due to the higher blood velocity through the TV in those cases. Finally, PVnoReg-ToF showed a spike in MKE at the end of diastole, attributable to the high-velocity regurgitant flow entering TV during its closure.

Low-velocity oscillations characterized the flow in the core of the systolic and diastolic jets, but high u'_{rms} were found in the shear layers and the proximity of the valves. The highest values (about $u'_{\text{rms}} = 0.1$ m/s) were reached at the peak E-wave within the shear layers of the tricuspid jets in the H scenario. In PVReg-ToF and PVnoReg-ToF cases, velocity oscillations had the same order of magnitude as the ensemble velocity, particularly at peak E-wave. Nonetheless, the highest values were recorded at the instant of maximum regurgitant pulmonary flow and were about 0.29 m/s and 0.63 m/s for PVReg-ToF and PVnoReg-ToF, respectively. Regarding the standard deviation, $\boldsymbol{\sigma}$, its patterns resembled those of u'_{rms} in all scenarios. The peak values of $\boldsymbol{\sigma}$ were identified during late diastole, at the peak A-wave, in the cases of H and PVnoReg-ToF, and corresponded approximately to 40% and 23% of the ensemble velocity, respectively. For PVReg-ToF, the peak values occurred during the early diastole, at the peak E-wave, and were around 20% of the ensemble velocity. Moreover, we identified the regions with high oscillatory behavior, $\|\boldsymbol{\sigma}\| > 0.1$ m/s, in the shear layers surrounding the tricuspid and pulmonary regurgitant jets (see Fig. 12). These flow regions are visualized in Fig. 12. Values of μ_{sgs}/μ displayed in Fig. 13 proved that the sigma-LES turbulence model is active in all three scenarios, especially within the RV in diastole. The μ_{sgs} reached the highest values during E-wave: about ten times greater than μ in H and more than 20 times in PVReg-ToF and PVnoReg-ToF.

Looking at the isosurfaces displayed in Fig. 13, ring vortices detaching from the PV leaflets were detected at peak systole. These vortices tended to rise along the pulmonary artery, and in the control case, they dissipated before reaching the outlet section, which is just before the pulmonary bifurcation plane. Additionally, below the TV, the typical "doughnut"-shaped vortex ring (ElBaz et al. 2014; Loke et al. 2022) developed in the H case at peak E-wave, and it

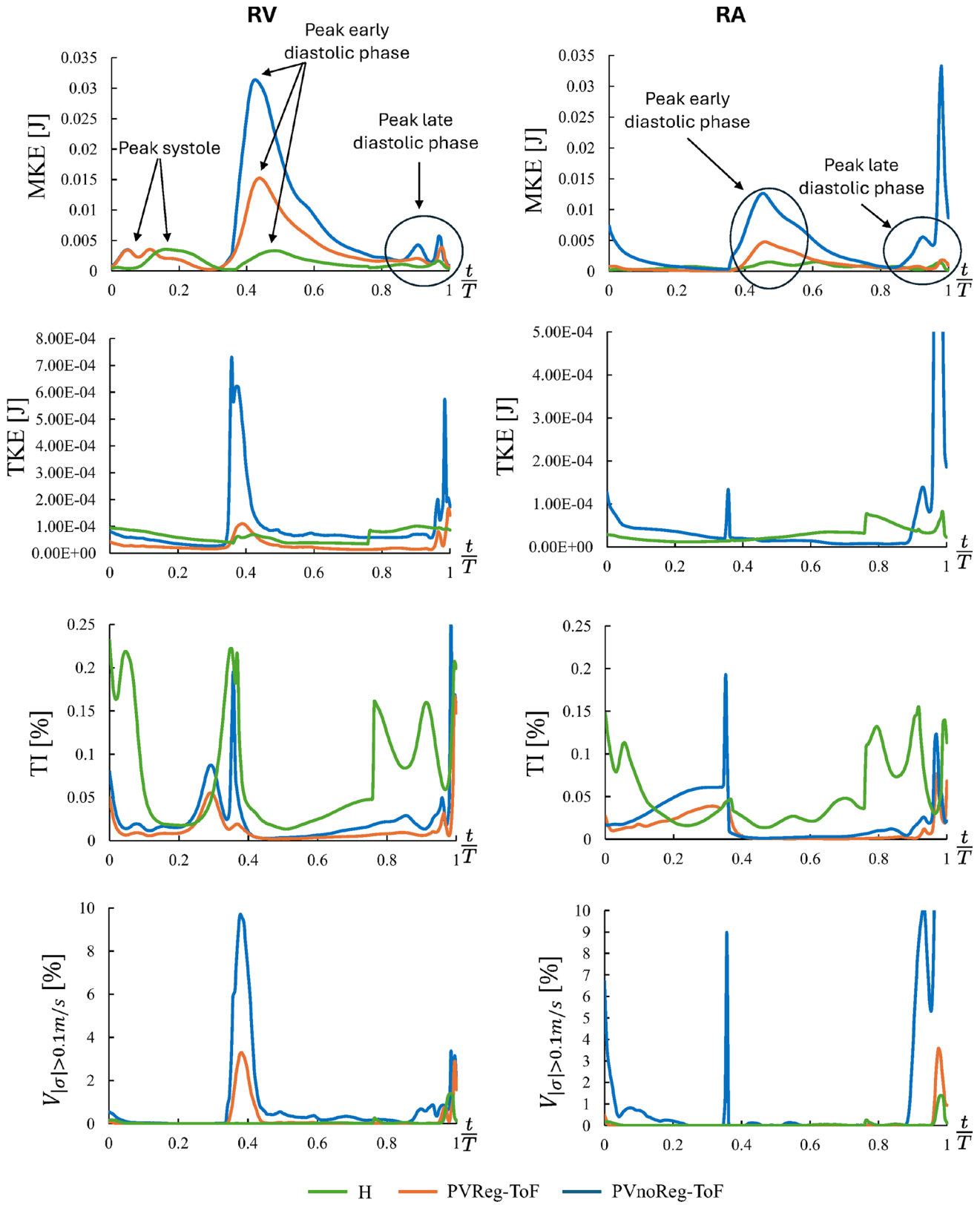

Fig. 11 First row: global mean kinetic energy; second row: global turbulent kinetic energy; third row: turbulence intensity; fourth row: volume percentage with standard deviation of the velocity fluctuations greater than 0.1 m/s. RV = right ventricle; RA = right atrium; H = control scenario; PVReg-ToF = pulmonary regurgitant repaired-ToF scenario; PVnoReg-ToF = postoperative non-regurgitant repaired-ToF scenario

Table 5 Reynolds numbers (Re) of tricuspid and pulmonary flows at four instant: t_{ps} represents peak systole; t_r is the instant of maximum pulmonary regurgitation; t_{Ew} represents peak E-wave; t_{Aw} represents peak A-wave

Scenario	t_{ps}	t_r	t_{Ew}	t_{Aw}
H	4300	–	2700	2400
PVReg-ToF	4100	3900	4700	1200
PVnoReg-ToF	4100	–	7300	1000

dissipated before reaching the ventricular apex. In PVReg-ToF case, the vortices originating from the two valves, though more extensive, also dissipated before reaching the RV apex. In contrast, in the PVnoReg-ToF scenario, the vorticose structure surrounding the tricuspid high-velocity jet extended all the way to the apex. Moreover, this case presented additional vortices within RA in systole and during the early diastole, which were consistent with flow streamlines depicted in Fig. 7. Despite these findings, the recorded TI remained below 0.3% and comparable with H within both RA and RV (see Fig. 11).

4.3 Analysis of wall stresses and stagnation risk

Wall shear stresses (WSS) for the three scenarios are illustrated in Fig. 14. Overall, WSS remained below 1 Pa throughout most of the heartbeat. However, peaks exceeding $2Pa$ were recorded in systole near the pulmonary leaflets' commissures and at the supraventricular crest in all scenarios. At peak E-wave in PVReg-ToF and PVnoReg-ToF cases, elevated stresses (about 2 Pa) were found in the anterior wall region where the high-velocity tricuspid jet impacts, as well as on the vascular walls of SVC and IVC due to increased inflow velocity. TAWSS results further proved that high WSS were transient. The highest TAWSS values stayed around 1 Pa, and it was observed on the RVOT wall near the PV annulus, on the pulmonary artery wall, and exclusively in the PVnoReg-ToF case, on the septal wall near TV. The regions where the flow was slow ($\|\langle \mathbf{u} \rangle\| < 0.2\,\mathrm{m/s}$), such as at the level of the ventricular apex, within RA, and within flow shear layers, exhibited high RRT values. In particular, RRT $> 10\ \mathrm{Pa}^{-1}$ was recorded at the apex and on RA wall in the H and PVReg-ToF scenarios. Conversely, in the PVnoReg-ToF case, the high-velocity tricuspid, SVC, and IVC flows effectively washed out these regions.

5 Discussion

5.1 Novelties of the present work

Characterizing flow within the right heart (RH) is particularly challenging due to its complex geometries. However, gaining insight into RH fluid dynamics is of extreme diagnostic importance because of the high incidence of acquired and congenital heart diseases with impaired RH functionality (Dumitrescu et al. 2018; Buechel and Mertens 2012; Haddad et al. 2008).

In this work, we carried out a computational study of the fluid dynamics of the RH. Our computational models were patient-specific and incorporated both chambers and valves with their motion. To the best of the authors' knowledge, this is the first work that addresses the analysis of fluid dynamics within a complete patient-specific RH model (RV + RA + TV + PV + PA) via DIB-CFD simulations. Moreover, as far as we are aware, this is the first computational study that includes the patient's TV reconstructed by images; prior works on RH hemodynamics typically modeled it by a planar surface (Loke et al. 2022; Wiputra et al. 2018).

Finally, we introduced a novel method that leverages information from all the available series to reconstruct the TV shape and motion from multiple cine MRI acquisitions. This allowed us to obtain patient-specific TV without relying on specific acquisitions, such as rotational cine MRI or three-dimensional echocardiography. Indeed, the proposed technique allowed for the first time, to obtain it by using only long-axis and two-/three-/four-chamber views. Owing to this, we were able, for the first time, to simulate the presence of mild tricuspid regurgitation in both healthy and pathological patient-specific scenarios, as well as the stenotic behavior of the repaired-ToF TV.

Notably, the proposed procedure can also be exploited for other dynamic images besides cine MRI, such as echocardiography, due to its flexibility with respect to the available medical images.

The results of our computational technique have been successfully compared with PC-MRI data at different time instants along the cardiac cycle (see Fig. 10). We notice that, interestingly, the accordance between measures and simulations is excellent at systole and diastole time instants t_1 and t_3, when the position of the leaflets is almost well defined, whereas some small discrepancies arise at the descending phase instant t_2, probably due to the movement of the closing leaflets. Although not providing a complete and definitive validation of our computational framework, this comparison highlights that our results have a significant real meaning.

5.2 Comparison between right and left ventricular hemodynamics

Our investigation highlighted key differences and commonalities between the RV and LV hemodynamics.

Similarly to the LV, the healthy RV generated a ring-shaped vortex during early diastole, which rolled up at the free margins of the TV leaflets. However, unlike in the LV, this RV vortex dissipates before reaching the apical region,

mainly due to the lower inertia of the tricuspid jet (ElBaz et al. 2014; Seo et al. 2014; Collia et al. 2021).

Despite these differences, the intraventricular hemodynamics is macroscopically similar between the left and right sides. As illustrated in Fig. 15, the inflow develops into two counter-rotating flows in both ventricles: a dominant one directed toward the outflow tract and a secondary, smaller one behind the valve leaflets. This flow pattern ensures that blood efficiently reaches the outflow and enters the circulatory system. However, these processes occur in two completely morphologically different chambers: an ellipsoid-like shape in LV and a "crescent" shape in RV. Consequently, the atrioventricular valve plays a crucial role in directing blood toward the semilunar valves, with their anatomy and morphology that are tailor-made to account for the different chambers' shapes.

Specifically, in RV, the chamber's curvature (in particular, at the level of the septum and of the crista terminalis) facilitates the blood flow into PA, after it impinges on the anterior wall; thus, a standard symmetric valve with three homogeneous leaflets is sufficient for ensuring the effective RV ejection. In contrast, the LV's nonstandard asymmetric valve with two completely different leaflets allows to avoid blood stagnation in the apical region. Indeed, it redirects the mitral jet to create a circulatory flow toward the aortic valve.

Furthermore, we observe that the presence of a second counter-rotating flow within the RV facilitates blood mixing of the apical blood particles, which are not reached by the main flow.

Finally, for sake of comparison with the LV literature, we computed the standard deviation of the fluctuations of the velocity magnitude, SD, as defined in Vergara et al. (2017) and Stella et al. (2019). We found that the peak value of this quantity during diastole was about $0.1 - 0.17\,\mathrm{m/s}$, corresponding to $25 - 33\%$ of the mean velocity. Similar results were detected within the left chamber in a recent work (Bennati et al. 2023a). This may suggest that, despite the hemodynamics conditions differ among LV and RV, namely intrachamber pressures and mean blood velocities, the mechanisms that regulate the balance between inertial and viscous forces act in such a way to ensure a comparable filling efficiency in healthy conditions.

5.3 Characterization of the regurgitant repaired-ToF hemodynamics

Thanks to our patient-specific DIB-CFD simulations, we were able to characterize in detail the complex pattern of the velocity field in both healthy and congenital RH (H and PVReg-ToF, respectively).

The two simulated scenarios differed in terms of chambers and valves' geometry and motion, as well as in terms of boundary conditions. These differences collectively contributed to determining their specific hemodynamics. For the PVReg-ToF case, a key distinctive feature is the development of a high-velocity jet through the TV at peak E-wave (see Fig. 6), which impinged on the RV lateral wall, causing a localized increase of WSS (see Fig. 14). The deflection of the diastolic jet toward the later ventricular wall, rather than the RVOT, partially contrasts with recent in vitro findings on the effect of pulmonary regurgitation on the fluid dynamics in repaired-ToF RV presented in Mikhail et al. (2020). This discrepancy may be attributable to the presence of the patient-specific valve in our model, which was not included in Mikhail et al. (2020). Indeed, it is know that the evolution of flow within the chambers is deeply affected by the valve morphology (Seo et al. 2014; Bennati et al. 2023b) together with the ventricular wall dynamics. Specifically, the PVReg-ToF TV was slightly stenotic compared to the healthy one ($\mathrm{TOA} = 4.36\,\mathrm{cm}^2$ against $10.1\,\mathrm{cm}^2$ of H scenario, Table 3), leading to a pressure drop across the valve of about 7 mmHg, which is outside the physiological ranges $1 - 3$ mmHg (Baumgartner et al. 2009) ($\Delta p = 2$ mmHg for H). Additionally, the cardiac motion determined very high TV flow at peak E-wave (see Table 4).

Another interesting topic related to the repaired-ToF simulation is represented by the atrium modeling. The reconstruction results highlighted the pathological behavior of the PVReg-ToF RA during diastole. In particular, Fig. 4 reveals the characteristic low compliance and increased conduit function that are typical features of a repaired-ToF RA (Kutty et al. 2017). By introducing the RA–RV coupling, we were able to reproduce the effects of this impaired RA function on the RV diastolic filling, which prolonged its diastasis phase. Moreover, effects were also observed on the TV closure dynamics, which lasted about 130 ms in the PVReg-ToF scenario against the 80 ms of H, as it can be deduced from the normalized times reported in Table 2. Embedding the patient-specific TV dynamics in the model also enabled us to capture the tricuspid regurgitation (TR) at the end of diastole (see Table 4). TR fell within the physiological ranges (Hahn et al. 2022) in both the H and PVReg-ToF cases. As far as we are aware, this is the first time that TR has been considered in CFD simulations despite its prevalence in 65–85% of the population (Arsalan et al. 2017). Given the high incidence of ToF, being able to computationally reproduce and analyze the effects of this condition on the intracardiac fluid dynamics can be a valuable tool in aiding surgical planning in view of avoiding irreversible RV damage in severe and chronic scenarios (Chorin et al. 2020).

Furthermore, the modeling of the entire RH system allowed us to detail the specific interplay between inflows from the superior and inferior vena cava (SVC and IVC, respectively), how the two sources of flow contribute to the regional ventricular filling, and how this interplay differs between healthy and pathological conditions. These results

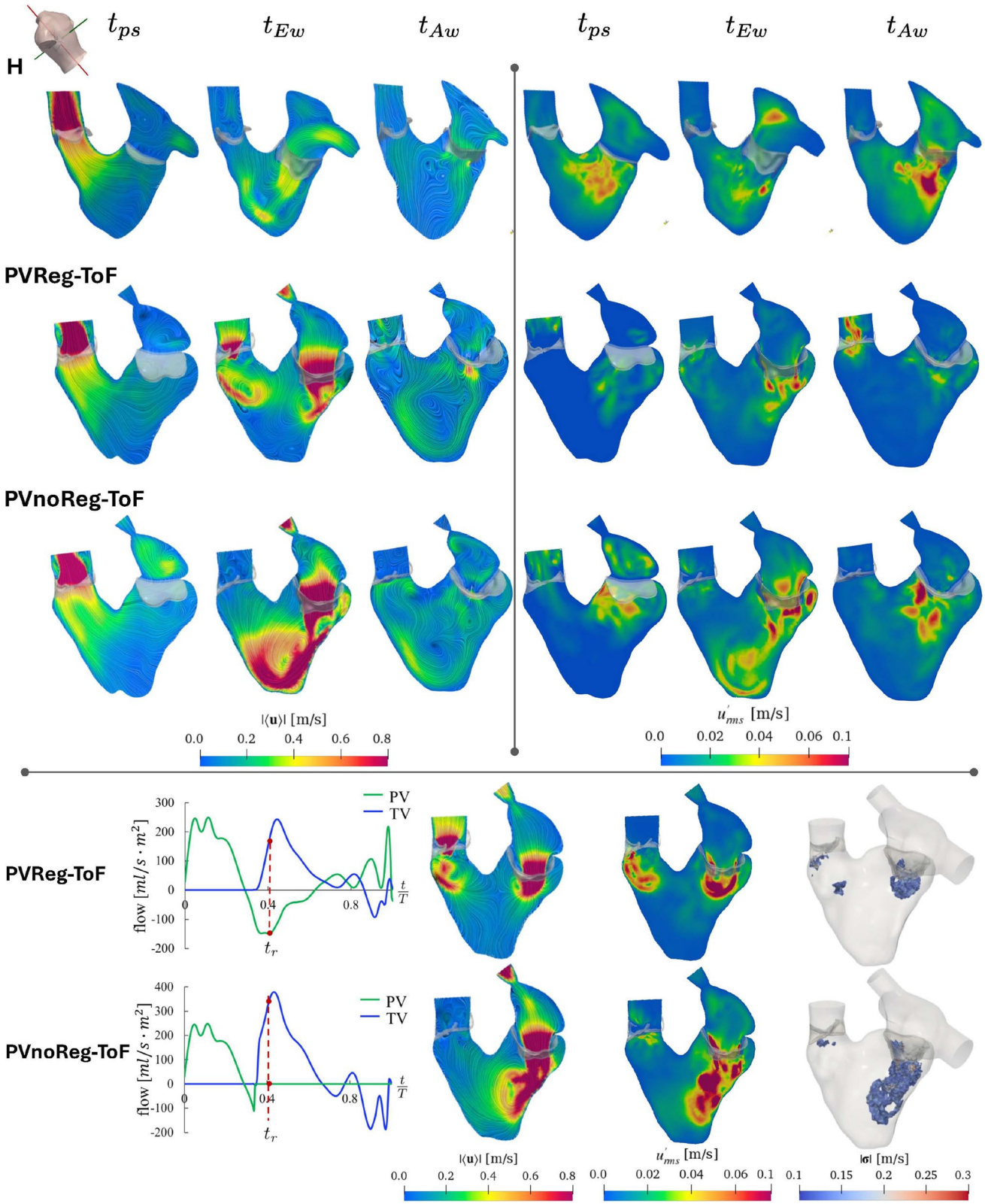
H
t_{ps}
t_{Ew}
t_{Aw}
t_{ps}
t_{Ew}
t_{Aw}
PVReg-ToF
PVnoReg-ToF
|⟨u⟩| [m/s]
0.0 0.2 0.4 0.6 0.8
u'_{rms} [m/s]
0.0 0.02 0.04 0.06 0.1
PVReg-ToF
PVnoReg-ToF
flow $[ml/s \cdot m^2]$
PV
TV
t_r
$\frac{t}{T}$
|⟨u⟩| [m/s]
0.0 0.2 0.4 0.6 0.8
u'_{rms} [m/s]
0.0 0.02 0.04 0.06 0.1
|σ| [m/s]
0.1 0.15 0.2 0.25 0.3

◂**Fig. 12** Visualization of quantities related to transition to turbulence. On the top, results are showed for all the scenarios at three relevant instants (peak systole, peak E-wave and peak A-wave). On the left: ensemble velocity magnitude on a slice; on the right: root mean square of the velocity fluctuations on the same slice. On the bottom, we report the results for PVReg-ToF and PVnoReg-ToF obtained at the instant t_r, when the former features its maximum pulmonary regurgitation. From left to right: flow rates at the valves' planes, magnitude of ensemble velocity, root mean square of the velocity fluctuations, and isosurfaces of standard deviation of the velocity fluctuations $\|\boldsymbol{\sigma}\| > 0.1\,\mathrm{m/s}$

were enhanced by the velocity streamlines depicted in Fig. 7 and were qualitatively in agreement with literature findings (François et al. 2012; ElBaz et al. 2014; Barker et al. 2019; Hudani et al. 2023) for both H and PVReg-ToF cases.

5.4 Characterization of transitional effects

Although the Reynolds numbers computed across valves in systole and diastole are quite high (see Table 5), approaching the upper limit of the transitional range (Yoganathan et al. 1988), we did not observe the complete transition to a fully turbulent regime in all the simulated scenarios. This can be attributable to the fact that the blood acceleration phases caused by the heart pulsatility tend to stabilize and laminarize the flow within the chambers in both systole and diastole.

Despite the absence of turbulence, there are still flow instabilities within the RA and RV, as showed by the pattern of velocity fluctuations and sub-grid-scale viscosity (see Figs. 12 and 13, respectively). Moreover, our highly detailed model allowed us to capture the vorticose structure that characterize the RV hemodynamics and energy exchange. The presence of these characteristic structures has been well documented in both the computational and clinical literature. Among all, we detected the main vortex that develops from TV (see Fig. 13) during diastole and that features a very regular ringlike shape in healthy RV scenario (François et al. 2012; ElBaz et al. 2014; Collia et al. 2021; Loke et al. 2024). In the PVReg-ToF case, this diastolic ring has a more elongated shape, which might be due to the higher jet velocity, the patient's TV shape (it is known that the leaflets of the atrioventricular valves orient the flow within the ventricle (Seo et al. 2014)), and the interaction with the pulmonary regurgitation jet as it was also detected in Loke et al. (2024). The diastolic vortex dissipates in both the healthy and pathological scenarios before reaching the RV apex. However, while for H, this dissipation is due to the relatively low Reynolds number (RE $\approx$ 2700) of the tricuspid jet, in the case of PVReg-ToF, it is due to the interaction with pulmonary vortices associated with the regurgitant jet.

We adopted the large eddy simulation σ model to describe and quantify the turbulent and transitional phenomena. This model has already proved to be suitable in simulating fluids in enclosed domain and in the presence of shear layers (Chnafa et al. 2016; Vergara et al. 2017). Although previous works described and quantified the turbulent energy and energy loss in the context of pulmonary regurgitant repaired-ToF (Collia et al. 2021; Loke et al. 2022, 2024), in this study we carried out an original analysis by exploring the contribution of the different scales to the distribution of energy within the healthy and pathological RH. In particular, by examining the global quantities, we observed that the PVReg-ToF presented a lower ratio between mean and turbulent kinetic energies (turbulent intensity, TI) compared to H, despite the higher Reynold numbers of its tricuspid and pulmonary jets (see Fig. 11). Notably, the peak values of the standard deviation of the velocity fluctuations (reported in Sect. 4.2) also reflected this trend as their percentage with respect to the ensemble velocity halved in PVReg-ToF as compared to the healthy scenario. At the same time, Fig. 13 shows a huge increase of the ratio between the sub-grid-scale viscosity and the molecular viscosity in the PVReg-ToF scenario, which suggests that the smallest scales contribute more to the dissipation of the turbulent energy with respect to H. In summary, in PVReg-ToF case, the laminar flow predominates over turbulence on the large scale since the velocity fluctuations are dampened by the rapid transfer of the turbulent energy toward the more active smallest scales. Conversely, within the healthy RH, the turbulent energy is more homogeneously distributed among the scales.

To conclude, the observed results suggested that the chaotic phenomena at the smallest scales are more pronounced in the pathological RH, where are mainly localized below the RVOT and the TV leaflets. This also could affect the forces exerted among the fluid layers and thus potentially damage blood cells or the cardiac wall endothelium (Lu et al. 2001).

5.5 Fluid dynamics changes induced by pulmonary valve replacement

To investigate the hemodynamics processes occurring immediately after PVR intervention in a repaired-ToF subject, we built a non-regurgitant repaired-ToF model (PVnoReg-ToF) on top of PVReg-ToF by replacing the regurgitant pulmonary valve with a competent one and by imposing customized pressure boundary conditions for the fluid problem (see Fig. 3).

We start by discussing our hypothesis that PVnoReg-ToF features the same endocardial displacement field as in PVReg-ToF, as well as its consequences on the numerical results. This assumption may not reflect a fair comparison between the two scenarios since, after PVR, no pulmonary regurgitation is expected and the ventricular volume curves should change accordingly. Specifically, we may expect reduced end-diastolic and end-systolic ventricular volumes

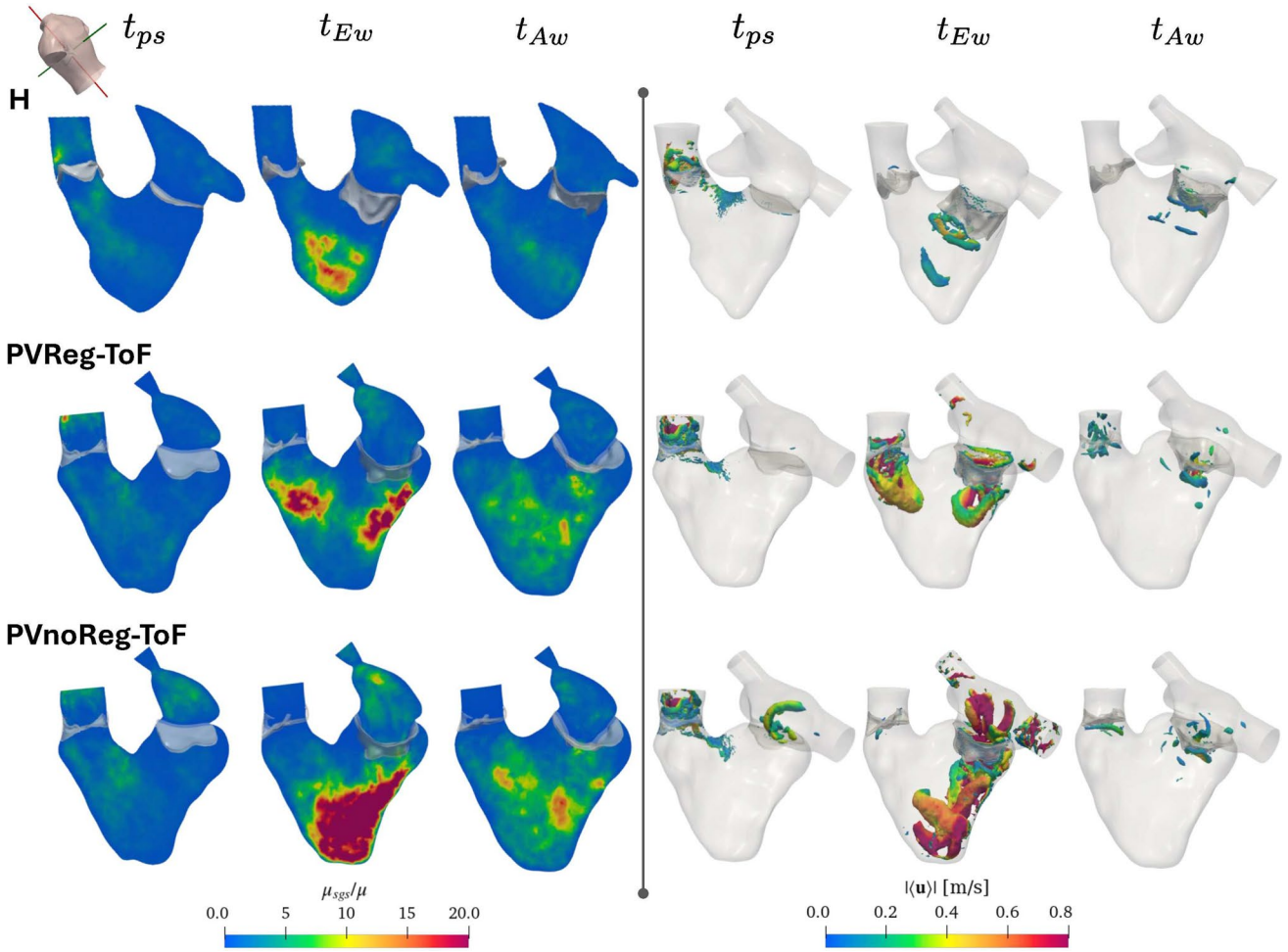

Fig. 13 On the left, the ratio between the sub-grid-scale viscosity and the molecular viscosity. On the right, vorticity isosurfaces representing the intracardiac flow, created with Q Criterion > 2000

in the post-PVR scenario (Lurz et al. 2009; Heng et al. 2017), reflecting a less dilated heart without suction effects. However, we can assume that, as the first approximation, immediately after the valve replacement the inertia of the beating heart maintains the same displacements of the regurgitant case. Only after a period of adjustment—which may last for a few minutes according to the study by Lurz et al. (2009)—the contraction will become almost physiological, with velocity patterns more similar to those observed in the healthy case (see Fig. 12). This justifies the meaningfulness of our results, at least for the acute regime.

The most marked effect of our hypothesis—using the same endocardial displacement of PVReg-ToF to PVnoReg-ToF, hence introducing an unphysiologically high filling through the TV to compensate for the perfect closure of the PV—was observed during diastole. Specifically, in PVnoReg-ToF, an increased flow rate through TV at peak E-wave, associated with elevated velocities and Reynolds numbers (Table 5 and Fig. 12). Moreover, the augmented kinetic energy of the jet, combined with the absence of the flow obstacle given by the pulmonary backflow, increased the RV penetration depth, which extended along the entire RV longitudinal dimension. Consequently, we observed higher WSS on the wall at the apex, though they remained transient (TAWSS values were below $0.2Pa$), and an enhancement, at the same time, of the apical blood washout (see Fig. 14). Additionally, flow instabilities grew within the overall RH, especially within RA, where vortical structures appeared already in diastole (see Figs. 11 and 13). Finally, during TV closure, the TR become moderate, increasing up to 17 ml/m^2 (Hahn et al. 2022).

These findings suggested that, immediately after the intervention, PVR leads to an increased cardiac output, with respect to the preoperative case, which may exceed the physiological needs of that patient after the adjustment induced by PVR. Although the presented results are still preliminary, the observed phenomena could be representative of an immediate post-intervention state and could trigger

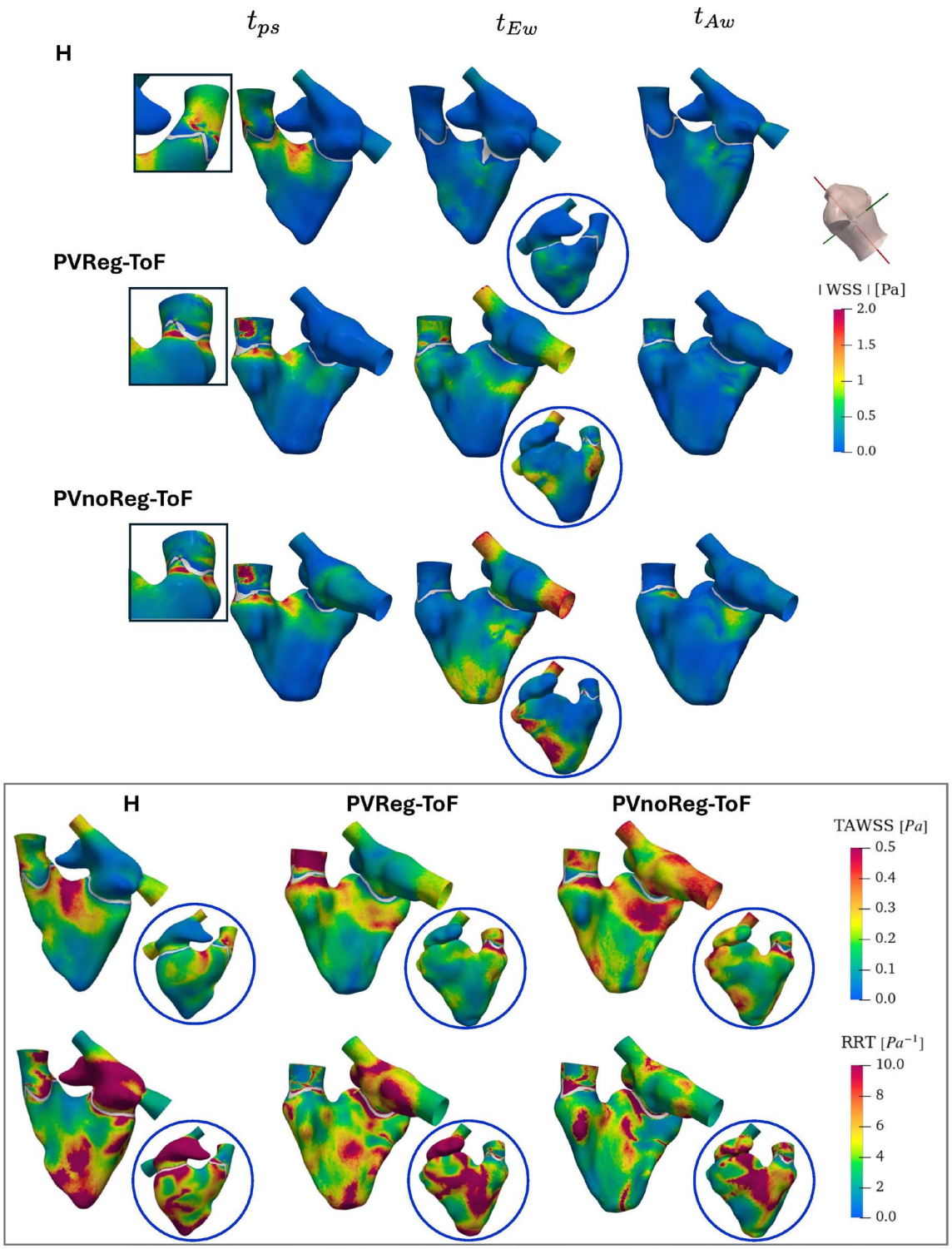

Fig. 14 Wall shear stresses and stagnation risk. On top, a representation of the 3D wall shear stress (WSS) patterns on the endocardial walls; square boxes: focus on the pulmonary commissures; round boxes: visualization of the anterior wall. Bottom panel: time averaged WSS (TAWSS) and relative residence time (RRT) patterns on the first and second rows, respectively, for the three scenarios

changes, especially in valve dynamics and cardiac motion, which may correlate with restoring RH functionality in repaired-ToF patients.

We finally observe that gaining insights into the mid- and long-term effects of PVR on repaired-ToF hemodynamics may require extending this work to investigate

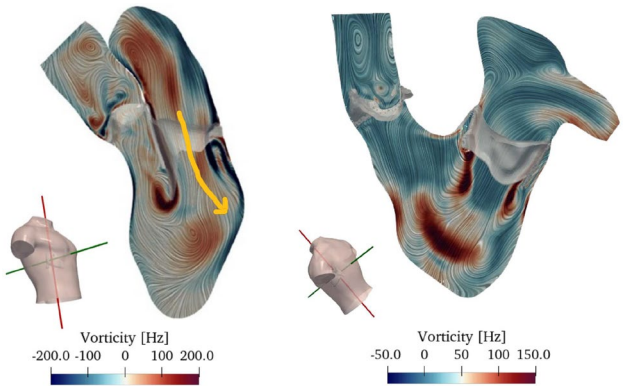

Fig. 15 Spatial distribution of the vorticity field at the peak of E-wave for two representative healthy cases: left heart of and aorta on the left; right heart and pulmonary artery on the right. Notice, highlighted by the yellow arrows, the straight inflow through the atrioventricular valve in the right ventricle, in contrast to the deflected blood flow entering the left ventricle, as a consequence of the asymmetric atrioventricular (mitral) valve. The latter picture has been modified from the PhD thesis by Lorenzo Bennati, University of Verona

blood–myocardium interactions, which play a key role in cardiac remodeling. This would require fluid–structure interaction analyses and/or the integration of long-term tissue remodeling models (Wang et al. 2017). A complementary or alternative approach is provided by recent proof-of-concept studies (Mojumder et al. 2023; Venet et al. 2024) using instantaneous models of ventricular myocardial mechanics, which allow for the quantification of chronic ventricular overload. This is an important factor of the reversible/irreversible tissue remodeling, hence possibly an important criterion for a timely PVR. We believe that incorporating such load assessments into the proposed CFD model could improve the interpretation of both hemodynamic changes and functional cardiac adaptation following PVR in repaired-ToF patients.

6 Limitations

Some limitations characterize this work:

1. We analyzed only two patients, one for each category. To support the considerations drawn in this work, we should consider a larger cohort of control subjects and repaired-ToF patients who underwent PVR. However, we believe that the presented results are very promising and could provide an excellent starting point for future studies;
2. Related to the previous point, it is important to note that this is a computational study rather than a statistical one. This means that we developed an a priori model based on the physical principles, as opposed to an a posteriori model based on data and measurements, which is typical in statistical approaches. Our aim was not to carry out extensive statistical analyses, given the relatively small sample size. Instead, we focused on providing a proof of concept to demonstrate the potential of the proposed methodology. This pipeline is particularly suited for systematic replication on a patient-specific basis;
3. Due to the absence of patients' clinical measurements, we could not validate our numerical results. Nonetheless, we demonstrated that our findings are both qualitatively and quantitatively consistent with the literature (Baumgartner et al. 2009; François et al. 2012; Barker et al. 2019; Hudani et al. 2023). This highlights the significance of our findings in the context of previous research, providing confidence in the validity of our conclusions despite the lack of direct clinical validation;
4. Since normal Neumann boundary conditions were imposed at the inlets of our DIB-CFD model, we could not reproduce the torsional motion of the SVC and IVC inflows (Parker et al. 2022). This limitation could influence the predicted blood velocity pattern and vortex formation within the right atrium. To address it, future studies should consider including additional MRI scans in the patient's imaging protocol to acquire the vena cava flows. These data could then be exploited either as boundary conditions for the CFD model or for validating the numerical results;
5. To study the PVnoReg-ToF scenario, we did not model the expected changes in atrial, ventricular, and tricuspid valve dynamics, which follow the restoration of pulmonary competence and may contribute to the inverse remodeling phenomenon (Heng et al. 2017). Including the post-PVR cardiac dynamics in the proposed model would have required the processing of post-implantation images, which were not available for this study. However, we believe that isolating the hemodynamic effects induced solely by the presence of a competent pulmonary valve still offers valuable insights into the underlying mechanisms of this process. A possible further development of our work in this direction would be the use of FSI models to also address blood–myocardium interactions involved in the cardiac remodeling phenomenon;
6. ToF patients are characterized by an asymmetrical flow partition among the two pulmonary arteries (Hudani et al. 2023), which could affect the downstream blood dynamics. However, we did not include the pulmonary bifurcation due to limitations of the acquired regions in the available cine MRI data;
7. We did not consider in our simulations the tricuspid and pulmonary valve coaptation regions, the sub-val-

vular apparatus, the pulmonary valve's lunule, and the ventricular trabeculations. This is a common choice in computational studies for RH (Wiputra et al. 2018; Collia et al. 2021; Loke et al. 2022) due to the challenges in accurately reconstructing the geometry and motion of these structures, which requires more spatially and temporally resolved imaging than cine MRI. Moreover, the inclusion of the sub-valvular apparatus in DIB-CFD models seems to have a minimal impact on the hemodynamics, at least not exactly near the leaflets (Crispino et al. 2024). Also, coaptation should not influence the systolic results sufficiently far from the leaflets. Additionally, the presence of trabeculations has been demonstrated to influence the vortex organization and WSS patterns, in particular at the level of the ventricular apex (Sacco et al. 2018), potentially affecting the local blood washout predictions. However, we think it is important to include such modeling features for future investigations;

8. Adapting a healthy valve (from the Zygote 3D heart model) to a diseased artery may represent a significant geometrical simplification potentially influencing the blood flow. In addition, uncertainties in the tricuspid valve reconstruction arising from the spatial and temporal resolution of the imaging data may further affect the reliability of the numerical results. For these reasons, future studies should investigate the effects of possible geometric variations in valve reconstruction on the right heart flow dynamics;
9. Handling the pulmonary valve dynamics through cosine interpolation between the fully open and fully closed valve configurations may introduce significant approximations, particularly in the diseased case, as the actual valve opening and closing processes occur rapidly and often involve fluttering around the open configuration. These phenomena may alter the local hemodynamics near the valve. To account for such phenomena in view of a more detailed description of valve hemodynamics, FSI and contact modeling approaches should be adopted in future studies;
10. Dangerous complications, which may appear over time, related to ToF patients are related to adverse electrophysiological events and the functioning of the pump due to the presence of scars and hypertrophy. Related to the second issue (hypertrophy), we notice that mathematical models for cardiac remodeling are nowadays too unripe and still underdeveloped to be applied to a clinical context. As for the first issue, an electrophysiological study accounting for scars or hypertrophy characterizing ToF patients would be possible, but it would require different imaging (able to detect scars or hypertrophy), it would not exploit the richness of time-resolved cine MRI data, and it would need different mathematical and numerical tools.

Acknowledgements FR and CV acknowledge their membership to INdAM GNCS—Gruppo Nazionale per il Calcolo Scientifico (National Group for Scientific Computing, Italy). FR has been partially supported by the INdAM GNCS project CUP E53C23001670001. CV has been partially supported by: (1) the European Union-Next Generation EU, Mission 4, Component 1, CUP: D53D23018770001, under the research project MIUR PRIN22-PNRR n.P20223KSS2, "Machine learning for fluid structure interaction in cardiovascular problems: efficient solutions, model reduction, inverse problems"; (2) the Italian Ministry of Health within the PNC PROGETTO HUB LIFE SCIENCE—DIAGNOSTICA AVANZATA (HLS-DA) "INNOVA," PNCE3—2022-23683266-CUP: D43C22004930001, within the "Piano Nazionale Complementare Ecosistema Innovativo della Salute"—Codice univoco investimento: PNCE3-2022-23683266; (3) the Italian research project MIUR PRIN22 n.2022L3JC5T "Predicting the outcome of endovascular repair for thoracic aortic aneurysms: analysis of fluid dynamic modeling in different anatomical settings and clinical validation"; and (4) Italian Ministry of Health within the project "CAL.HUB.RIA"—CALABRIA HUB PER RICERCA INNOVATIVA ED AVANZATA. Code: T4-AN-09, CUP: F63C22000530001. The authors acknowledge the CINECA award under the ISCRA initiative, for the availability of high-performance computing resources and support.

Author contributions GP acquired the clinical data. FR and CV contributed to the methodology. FR did the image reconstruction and the numerical simulations, carried out the formal analysis and investigation, and participated in writing—the original draft preparation. FR, GP, GBL, and CV conceived the study. FR and CV contributed to the formal analysis, investigation, and interpretation of the results. CV, GP, and GBL took part in writing—review and editing. CV and GBL were involved in the supervision of the study

Declarations

Conflict of interest No conflict of interest, financial or otherwise, are declared by the authors.

Ethical approval Ethical review board gave approval for this study, and informed consent was obtained from all patients.

References

Abozied OA, Deshmukh AJ, Younis A, Ahmed M, Luke Burchill C, Jain C, Miranda WR, Madhavan M, Connolly HM, Egbe AC (2024) Right atrial reverse remodeling and risk of atrial arrhythmias after surgical pulmonary valve replacement. Int J Cardiol Congenit Heart Dis 15:100497. https://doi.org/10.1016/j.ijcchd.2024.100497

Africa PC (2022) lifex: A flexible, high performance library for the numerical solution of complex finite element problems. SoftwareX 20:101252. https://doi.org/10.1016/j.softx.2022.101252

Africa PC, Fumagalli I, Bucelli M, Zingaro A, Fedele M, Dede' L, Quarteroni A (2024) lifex-cfd: An open-source computational fluid dynamics solver for cardiovascular applications. Comput Phys Commun 296:109039. https://doi.org/10.1016/j.cpc.2023.109039. (**ISSN 0010-4655**)

Ait-ALi L, Marrone C, Salvadori S, Federici D, Pak V, Arcieri L, Passino C, Santoro G, Festa P (2020) Impact of right atrium

dimension on adverse outcome after pulmonary valve replacement in repaired tetralogy of Fallot patients. Int J Cardiovasc Imaging 36(10):1973–1982. https://doi.org/10.1007/s10554-020-01891-9

Ali LA, Lurz P, Ripoli A, Rossi G, Kister T, Aquaro GD, Passino C, Bonhoeffer P, Festa P (2019) Implications of atrial volumes in surgical corrected tetralogy of Fallot on clinical adverse events. Int J Cardiol 283:107–111. https://doi.org/10.1016/j.ijcard.2019.02.018

Antiga L, Piccinelli M, Botti L, Ene-Iordache B, Remuzzi A, Steinman DA (2008) An image-based modeling framework for patient-specific computational hemodynamics. Med Biol Eng Comput 46:1097–1112. https://doi.org/10.1007/s11517-008-0420-1

Arndt D, Bangerth W, Feder M, Fehling M, Gassmöller R, Heister T, Heltai L, Kronbichler M, Maier M, Munch P et al (2022) The deal. ii library, version 9.4. J Numer Math 30(3):231–246. https://doi.org/10.1515/jnma-2022-0054

Arsalan M, Walther T, Smith RL, Grayburn PA (2017) Tricuspid regurgitation diagnosis and treatment. Eur Heart J 38(9):634–638. https://doi.org/10.1093/eurheartj/ehv487

Augustin CM, Crozier A, Neic A, Prassl AJ, Karabelas E, Ferreira da Silva T, Fernandes JF, Campos F, Kuehne T, Plank G (2016) Patient-specific modeling of left ventricular electromechanics as a driver for haemodynamic analysis. EP Eur 18(suppl 4):iv121–iv129. https://doi.org/10.1093/europace/euw369

Barker N, Fidock B, Johns CS, Kaur H, Archer G, Rajaram S, Hill C, Thomas S, Karunasaagarar K, Capener D et al (2019) A systematic review of right ventricular diastolic assessment by 4d flow CMR. Biomed Res Int 2019(1):6074984. https://doi.org/10.1155/2019/6074984

Baumgartner H, Hung J, Bermejo J, Chambers JB, Evangelista A, Griffin BP, Iung B, Otto CM, Pellikka PA, Quiñones M (2009) Echocardiographic assessment of valve stenosis: Eae/ase recommendations for clinical practice. Eur J Echocardiogr 10(1):1–25. https://doi.org/10.1016/j.echo.2008.11.029

Bennati L, Giambruno V, Renzi F, Di Nicola V, Maffeis C, Puppini G, Luciani GB, Vergara C (2023) Turbulent blood dynamics in the left heart in the presence of mitral regurgitation: a computational study based on multi-series cine-MRI. Biomech Model Mechanobiol 22(6):1829–1846. https://doi.org/10.1007/s10237-023-01735-0

Bennati L, Vergara C, Giambruno V, Fumagalli I, Corno AF, Quarteroni A, Puppini G, Luciani GB (2023) An image-based computational fluid dynamics study of mitral regurgitation in presence of prolapse. Cardiovasc Eng Technol 14(3):457–475. https://doi.org/10.1007/s13239-023-00665-3

Biglino G, Capelli C, Bruse J, Bosi GM, Taylor AM, Schievano S (2017) Computational modelling for congenital heart disease: how far are we from clinical translation? Heart 103(2):98–103. https://doi.org/10.1136/heartjnl-2016-310423

Bucelli M, Zingaro A, Africa PC, Fumagalli I, Dede' L, Quarteroni A (2023) A mathematical model that integrates cardiac electrophysiology, mechanics, and fluid dynamics: application to the human left heart. Int J Numer Methods Biomed Eng 39(3):e3678. https://doi.org/10.1002/cnm.3678

Chnafa C, Mendez S, Nicoud F (2016) Image-based simulations show important flow fluctuations in a normal left ventricle: what could be the implications? Ann Biomed Eng 44:3346–3358. https://doi.org/10.1007/s10439-016-1614-6

Chorin E, Rozenbaum Z, Topilsky Y, Konigstein M, Ziv-Baran T, Richert E, Keren G, Banai S (2020) Tricuspid regurgitation and long-term clinical outcomes. Eur Heart J-Cardiovascular Imaging 21(2):157–165. https://doi.org/10.1093/ehjci/jez216

Collia D, Zovatto L, Tonti G, Pedrizzetti G (2021) Comparative analysis of right ventricle fluid dynamics. Front Bioeng Biotechnol 9:667408. https://doi.org/10.3389/fbioe.2021.667408

Elisabetta C, Ivan F, Alfio Q, Maria MS, Christian V (2024) Computational haemodynamics for pulmonary valve replacement by means of a reduced fluid-structure interaction model. Int J Numer Methods Biomed Eng. https://doi.org/10.1002/cnm.3846

Crispino A, Bennati L, Vergara C (2024) Cardiac hemodynamics computational modeling including chordae tendineae, papillaries, and valves dynamics. bioRxiv, pp 2024–05, https://doi.org/10.1101/2024.05.21.595150

Cuypers J, Menting ME, Konings E, Opić P, Utens E, Helbing WA, Witsenburg M, van den Bosch AE, Ouhlous M, van Domburg RT et al (2014) Unnatural history of tetralogy of Fallot: prospective follow-up of 40 years after surgical correction. Circulation 130(22):1944–1953. https://doi.org/10.1161/CIRCULATIONAHA.114.009454

Das A, Banerjee RK, Gottliebson WM (2010) Right ventricular inefficiency in repaired tetralogy of Fallot: proof of concept for energy calculations from cardiac MRI data. Ann Biomed Eng 38:3674–3687. https://doi.org/10.1007/s10439-010-0107-2

de Oliveira DC, Owen DG, Qian S, Green NC, Espino DM, Shepherd D (2021) Computational fluid dynamics of the right atrium: assessment of modelling criteria for the evaluation of dialysis catheters. PLoS ONE 16(2):e0247438. https://doi.org/10.1371/journal.pone.0247438

Dumitrescu SI, Ţintoiu IC, Underwood MJ (2018) Right Heart Pathology: From Mechanism to Management. Springer, ISBN 978-3-319-73763-8. https://doi.org/10.1007/978-3-319-73764-5

Egbe AC, Bonnichsen C, Reddy Y, Anderson JH, Borlaug BA (2019) Pathophysiologic and prognostic implications of right atrial hypertension in adults with tetralogy of Fallot. J Am Heart Assoc 8(22):e014148. https://doi.org/10.1161/JAHA.119.014148

ElBaz MS, Calkoen E, Westenberg JJ, Lelieveldt B, Roest A, van der Geest RJ (2014) Three dimensional right ventricular diastolic vortex rings: characterization and comparison with left ventricular diastolic vortex rings from 4d flow MRI. J Cardiovasc Magn Reson 16:1–3. https://doi.org/10.1186/1532-429X-16-S1-P42

Fedele M, Quarteroni A (2021) Polygonal surface processing and mesh generation tools for the numerical simulation of the cardiac function. Int J Numer Methods Biomed Eng 37(4):e3435. https://doi.org/10.1002/cnm.3435

Fedele M, Faggiano E, Dedè L, Quarteroni A (2017) A patient-specific aortic valve model based on moving resistive immersed implicit surfaces. Biomech Model Mechanobiol 16:1779–1803. https://doi.org/10.1007/s10237-017-0919-1

Fernández MA, Gerbeau J-F, Martin V (2008) Numerical simulation of blood flows through a porous interface. ESAIM: Math Model Numer Anal 42(6):961–990. https://doi.org/10.1051/m2an:2008031

François CJ, Srinivasan S, Schiebler ML, Reeder SB, Niespodzany E, Landgraf BR, Wieben O, Frydrychowicz A (2012) 4d cardiovascular magnetic resonance velocity mapping of alterations of right heart flow patterns and main pulmonary artery hemodynamics in tetralogy of Fallot. J Cardiovasc Magn Reson 14(1):11. https://doi.org/10.1186/1532-429X-14-16

Freling HG, Willems TP, van Melle JP, van Slooten YJ, Bartelds B, Berger R, van Veldhuisen DJ, Pieper PG (2014) Effect of right ventricular outflow tract obstruction on right ventricular volumes and exercise capacity in patients with repaired tetralogy of Fallot. Am J Cardiol 113(4):719–723. https://doi.org/10.1016/j.amjcard.2013.10.049

Fumagalli I, Fedele M, Vergara C, Ippolito S, Nicolò F, Antona C, Scrofani R, Quarteroni A et al (2020) An image-based computational hemodynamics study of the systolic anterior motion of the mitral valve. Comput Biol Med 123:103922. https://doi.org/10.1016/j.compbiomed.2020.103922

Ivan F, Piermario V, Christian V, Marco F, Corno AF, Sonia I, Roberto S, Alfio Q (2022) Image-based computational hemodynamics analysis of systolic obstruction in hypertrophic cardiomyopathy. Front Physiol. https://doi.org/10.3389/fphys.2021.787082

Fumagalli I, Pagani S, Vergara C, Adebo DA, Del Greco M, Frontera A, Luciani GB, Pontone G, Scrofani R, Quarteroni A et al (2024) The role of computational methods in cardiovascular medicine: a narrative review. Translat Pediatr 13(1):146. https://doi.org/10.21037/tp-23-184

Grignola JC (2011) Hemodynamic assessment of pulmonary hypertension. World J Cardiol 3(1):10. https://doi.org/10.4330/wjc.v3.i1.10

Haddad F, Doyle R, Murphy DJ, Hunt SA (2008) Right ventricular function in cardiovascular disease, part ii: pathophysiology, clinical importance, and management of right ventricular failure. Circulation 117(13):1717–1731. https://doi.org/10.1161/CIRCULATIONAHA.107.653584

Hahn RT, Badano LP, Bartko PE, Muraru D, Maisano F, Zamorano JL, Donal E (2022) Tricuspid regurgitation: recent advances in understanding pathophysiology, severity grading and outcome. Eur Heart J-Cardiovasc Imaging 23(7):913–929. https://doi.org/10.1093/ehjci/jeac009

Heng EL, Gatzoulis MA, Uebing A, Sethia B, Uemura H, Smith GC, Diller G-P, McCarthy KP, Ho SY, Li W et al (2017) Immediate and midterm cardiac remodeling after surgical pulmonary valve replacement in adults with repaired tetralogy of Fallot: a prospective cardiovascular magnetic resonance and clinical study. Circulation 136(18):1703–1713. https://doi.org/10.1161/CIRCULATIONAHA.117.027402

Himburg HA, Grzybowski DM, Hazel AL, LaMack JA, Li X-M, Friedman MH (2004) Spatial comparison between wall shear stress measures and porcine arterial endothelial permeability. Am J Physiol-Heart Circulatory Physiol 286(5):H1916–H1922. https://doi.org/10.1152/ajpheart.00897.2003

Hirt CW, Amsden AA, Cook JL (1997) An arbitrary Lagrangian-Eulerian computing method for all flow speeds. J Comput Phys 135(2):203–216. https://doi.org/10.1006/jcph.1997.5702

Hudani A, Ali SI, Patton D, Myers KA, Fine NM, White JA, Greenway S, Garcia J (2023) 4d-flow MRI characterization of pulmonary flow in repaired tetralogy of Fallot. Appl Sci 13(5):2810. https://doi.org/10.3390/app13052810

Katritsis D, Kaiktsis L, Chaniotis A, Pantos J, Efstathopoulos EP, Marmarelis V (2007) Wall shear stress: theoretical considerations and methods of measurement. Prog Cardiovasc Dis 49(5):307–329. https://doi.org/10.1016/j.pcad.2006.11.001

Kutty S, Shang Q, Joseph N, Kowallick JT, Schuster A, Steinmetz M, Danford DA, Beerbaum P, Sarikouch S (2017) Abnormal right atrial performance in repaired tetralogy of Fallot: A CMR feature tracking analysis. Int J Cardiol 248:136–142. https://doi.org/10.1016/j.ijcard.2017.06.121

Lev M, Eckner F (1964) The pathologic anatomy of tetralogy of Fallot and its variations. Dis Chest 45(3):251–261. https://doi.org/10.1378/chest.45.3.251

Litovsky S, Choy M, Park J, Parrish M, Waters B, Nagashima M, Van Praagh R, Van Praagh S (2000) Absent pulmonary valve with tricuspid atresia or severe tricuspid stenosis: report of three cases and review of the literature. Pediatr Dev Pathol 3:353–366. https://doi.org/10.1007/s100249910050

Loke Y-H, Capuano F, Balaras E, Olivieri LJ (2022) Computational modeling of right ventricular motion and intracardiac flow in repaired tetralogy of Fallot. Cardiovasc Eng Technol 13(1):41–54. https://doi.org/10.1007/s13239-021-00558-3

Loke Y-H, Yildiran IN, Capuano F, Balaras E, Olivieri L (2024) Tetralogy of Fallot regurgitation energetics and kinetics: an intracardiac flow analysis of the right ventricle using computational fluid dynamics. Int J Cardiovasc Imaging. https://doi.org/10.1007/s10554-024-03084-0

Lu PC, Lai HC, Liu JS (2001) A reevaluation and discussion on the threshold limit for hemolysis in a turbulent shear flow. J Biomech 34(10):1361–1364. https://doi.org/10.1016/S0021-9290(01)00084-7

Lurz P, Nordmeyer J, Muthurangu V, Khambadkone S, Derrick G, Yates R, Sury M, Bonhoeffer P, Taylor AM (2009) Comparison of bare metal stenting and percutaneous pulmonary valve implantation for treatment of right ventricular outflow tract obstruction: use of an x-ray/magnetic resonance hybrid laboratory for acute physiological assessment. Circulation 119(23):2995–3001. https://doi.org/10.1161/CIRCULATIONAHA.108.836312

Mangual JO, Domenichini F, Pedrizzetti G (2012) Describing the highly three dimensional right ventricle flow. Ann Biomed Eng 40(8):1790–1801. https://doi.org/10.1007/s10439-012-0540-5

Mareels G, De Wachter DS, Verdonck PR (2004) Computational fluid dynamics-analysis of the Niagara hemodialysis catheter in a right heart model. Artif Organs 28(7):639–648. https://doi.org/10.1111/j.1525-1594.2004.07371.x

Mikhail A, Di Labbio G, Darwish A, Kadem L (2020) How pulmonary valve regurgitation after tetralogy of Fallot repair changes the flow dynamics in the right ventricle: An in vitro study. Med Eng Phys 83:48–55. https://doi.org/10.1016/j.medengphy.2020.07.014

Mohr R, Smolinsky A, Ziskind Z, Quang HT, Goor D (1986) Negative right ventricular diastolic pressure after operation for pulmonary valve stenosis: the phenomenon and its relation to volume load and conal contraction. Heart 55(1):92–96

Mojumder J, Fan L, Nguyen T, Campbell KS, Wenk JF, Guccione JM, Abraham T, Lee LC (2023) Computational analysis of ventricular mechanics in hypertrophic cardiomyopathy patients. Sci Rep 13(1):958. https://doi.org/10.1038/s41598-023-28037-w

Nanda NC, Gramiak R, Robinson TI, Shah PM (1974) Echocardiographic evaluation of pulmonary hypertension. Circulation 50(3):575–581. https://doi.org/10.1161/01.CIR.50.3.575

Nicoud F, Toda HB, Cabrit O, Bose S, Lee J (2011) Using singular values to build a subgrid-scale model for large eddy simulations. Phys Fluids 23(8):085106. https://doi.org/10.1063/1.3623274

Nobile F, Formaggia L (1999) A stability analysis for the arbitrary Lagrangian Eulerian formulation with finite elements. East-West J Numer Math 7:105–132

Pappano AJ, Wier WG (2018) Cardiovascular physiology-e-book. Elsevier Health Sciences, ISBN 978-0-323-08697-4

Parker LP, Marcial AS, Brismar TB, Broman LM, Wittberg LP (2022) Impact of altered vena cava flow rates on right atrium flow characteristics. J Appl Physiol 132(5):1167–1178. https://doi.org/10.1152/japplphysiol.00649.2021

Pass RH, Cohen J (2023) Tetralogy of Fallot. pp 1–23. https://doi.org/10.1007/978-3-030-42937-9_55-1

Pope SB (2001) Turbulent flows, vol 12. https://doi.org/10.1088/0957-0233/12/11/705

Quarteroni A, Manzoni A, Vergara C et al (2019) Mathematical modelling of the human cardiovascular system: data, numerical approximation, clinical applications, vol 33. Cambridge University Press, Cambridge (**ISBN 9781108480390**)

Redington AN (2006) Determinants and assessment of pulmonary regurgitation in tetralogy of Fallot: practice and pitfalls. Cardiol Clin 24(4):631–639. https://doi.org/10.1016/j.ccl.2006.08.007

Renzi F, Vergara C, Fedele M, Giambruno V, Quarteroni A, Puppini G, Luciani GB (2025) Accurate reconstruction of right heart shape and motion from cine-MRI for image-driven computational hemodynamics. Int J Numer Methods Biomed Eng 41(1):e3891. https://doi.org/10.1002/cnm.3891

Riccardello Jr GJ, Shastri DN, Changa AR, Thomas KG, Roman M, Prestigiacomo CJ, Gandhi CD (2018) Influence of relative residence time on side-wall aneurysm inception. Neurosurgery 83(3):574–581. https://doi.org/10.1093/neuros/nyx433

Sacco F, Paun B, Lehmkuhl O, Iles TL, Iaizzo PA, Houzeaux G, Vázquez M, Butakoff C, Aguado-Sierra J (2018) Evaluating the roles of detailed endocardial structures on right ventricular

haemodynamics by means of CFD simulations. Int J Numer Methods Biomed Eng 34(9):e3115. https://doi.org/10.1002/cnm.3115
Scott DB (1963) Inferior vena caval pressure: changes occurring during anaesthesia. Anaesthesia 18(2):135–142
Senthilnathan S, Dragulescu A, Mertens L (2013) Pulmonary regurgitation after tetralogy of Fallot repair: a diagnostic and therapeutic challenge. J Cardiovasc Echogr 23(1):1–9. https://doi.org/10.4103/2211-4122.117975
Seo JH, Vedula V, Abraham T, Lardo AC, Dawoud F, Luo H, Mittal R (2014) Effect of the mitral valve on diastolic flow patterns. Phys Fluids. doi 10(1063/1):4904094. https://doi.org/10.1063/1.4904094
Stein K, Tezduyar T, Benney R (2003) Mesh moving techniques for fluid-structure interactions with large displacements. J Appl Mech 70(1):58–63. https://doi.org/10.1115/1.1530635
Stella S, Vergara C, Giovannacci L, Quarteroni A, Prouse G (2019) Assessing the disturbed flow and the transition to turbulence in the arteriovenous fistula. J Biomech Eng 141(10):101010. https://doi.org/10.1115/1.4043448
Stevanella M, Maffessanti F, Conti CA, Votta E, Arnoldi A, Lombardi M, Parodi O, Caiani EG, Redaelli A (2011) Mitral valve patient-specific finite element modeling from cardiac MRI: application to an annuloplasty procedure. Cardiovasc Eng Technol 2:66–76. https://doi.org/10.1007/s13239-010-0032-4
Tang D, Yang C, Geva T, Pedro J (2010) Image-based patient-specific ventricle models with fluid-structure interaction for cardiac function assessment and surgical design optimization. Prog Pediatr Cardiol 30(1–2):51–62. https://doi.org/10.1016/j.ppedcard.2010.09.007
Tezduyar TE, Senga M (2006) Stabilization and shock-capturing parameters in SUPG formulation of compressible flows. Comput Methods Appl Mech Eng 195(13–16):1621–1632. https://doi.org/10.1016/j.cma.2005.05.032
This A, Boilevin-Kayl L, Fernández MA, Gerbeau J-F (2020) Augmented resistive immersed surfaces valve model for the simulation of cardiac hemodynamics with isovolumetric phases. Int J Numer Methods Biomed Eng 36(3):e3223. https://doi.org/10.1002/cnm.3223
Valsangiacomo Buechel ER, Mertens LL (2012) Imaging the right heart: the use of integrated multimodality imaging. Eur Heart J 33(8):949–960. https://doi.org/10.1093/eurheartj/ehr490
Venet M, Malik A, Gold S, Zhang N, Gopaul J, Dauz J, Yazaki K, Ponzoni M, Coles JG, Maynes JT et al (2024) Impact of right ventricular pressure overload on myocardial stiffness assessed by natural wave imaging. JACC: Cardiovasc Imaging. https://doi.org/10.1016/j.jcmg.2024.06.020
Vergara C, Le Van D, Quadrio M, Formaggia L, Domanin M (2017) Large eddy simulations of blood dynamics in abdominal aortic aneurysms. Med Eng Phys 47:38–46. https://doi.org/10.1016/j.medengphy.2017.06.030
Viola F, Spandan V, Meschini V, Romero J, Fatica M, de Tullio MD, Verzicco R (2022) FSEI-GPU: Gpu accelerated simulations of the fluid-structure-electrophysiology interaction in the left heart. Comput Phys Commun 273:108248. https://doi.org/10.1016/j.cpc.2021.108248
Votta E, Caiani E, Veronesi F, Soncini M, Montevecchi FM, Redaelli A (2008) Mitral valve finite-element modelling from ultrasound data: a pilot study for a new approach to understand mitral function and clinical scenarios. Philos Trans R Soc A: Math, Phys Eng Sci 366(1879):3411–3434. https://doi.org/10.1098/rsta.2008.0095
Wang VY, Hussan JR, Yousefi H, Bradley CP, Hunter PJ, Nash MP (2017) Modelling cardiac tissue growth and remodelling. J Elast 129:283–305. https://doi.org/10.1007/s10659-017-9640-7
Wiputra H, Lai CQ, Lim GL, Heng J, Guo L, Soomar SM, Leo HL, Biwas A, Mattar C, Yap CH (2016) Fluid mechanics of human fetal right ventricles from image-based computational fluid dynamics using 4d clinical ultrasound scans. Am J Physiol-Heart Circ Physiol 311(6):H1498–H1508. https://doi.org/10.1152/ajpheart.00400.2016
Wiputra H, Chen CK, Talbi E, Lim GL, Soomar SM, Biswas A, Mattar C, Bark D, Leo HL, Yap CH (2018) Human fetal hearts with tetralogy of Fallot have altered fluid dynamics and forces. Am J Physiol-Heart Circ Physiol 315(6):H1649–H1659. https://doi.org/10.1152/ajpheart.00235.2018
Yoganathan AP, Cape EG, Sung H-W, Williams FP, Jimoh A (1988) Review of hydrodynamic principles for the cardiologist: applications to the study of blood flow and jets by imaging techniques. J Am Coll Cardiol 12(5):1344–1353. https://doi.org/10.1016/0735-1097(88)92620-4
Zingaro A, Bucelli M, Piersanti R, Regazzoni F, Quarteroni A et al (2024) An electromechanics-driven fluid dynamics model for the simulation of the whole human heart. J Comput Phys 504:112885. https://doi.org/10.1016/j.jcp.2024.112885